




# In situ characterization on macroscale 3D spatial dispersion of MWCNTs in matrix and interfacial phases of quartz fibers/epoxy composites via fluorescence imaging

Cong Liu<sup>1</sup>, Liu Meng<sup>1</sup>, Xianhua Huan<sup>1</sup>, Hefeng Li<sup>1</sup>, Jintao Luo<sup>1</sup>, Rongrong Xie<sup>1</sup>, Wenqiao Zhang<sup>1</sup>, Xiaolong Jia<sup>1,2,\*</sup> , Qing Cai<sup>1</sup>, and Xiaoping Yang<sup>1,2</sup>

<sup>1</sup> State Key Laboratory of Organic-Inorganic Composites, College of Materials Science and Engineering, Beijing University of Chemical Technology, Beijing 100029, People's Republic of China

<sup>2</sup> Key Laboratory of Carbon Fiber and Functional Polymer, Beijing University of Chemical Technology, Ministry of Education, Beijing 100029, People's Republic of China

Received: 7 April 2021

Accepted: 13 July 2021

Published online:

28 July 2021

© The Author(s), under exclusive licence to Springer Science+Business Media, LLC, part of Springer Nature 2021

## ABSTRACT

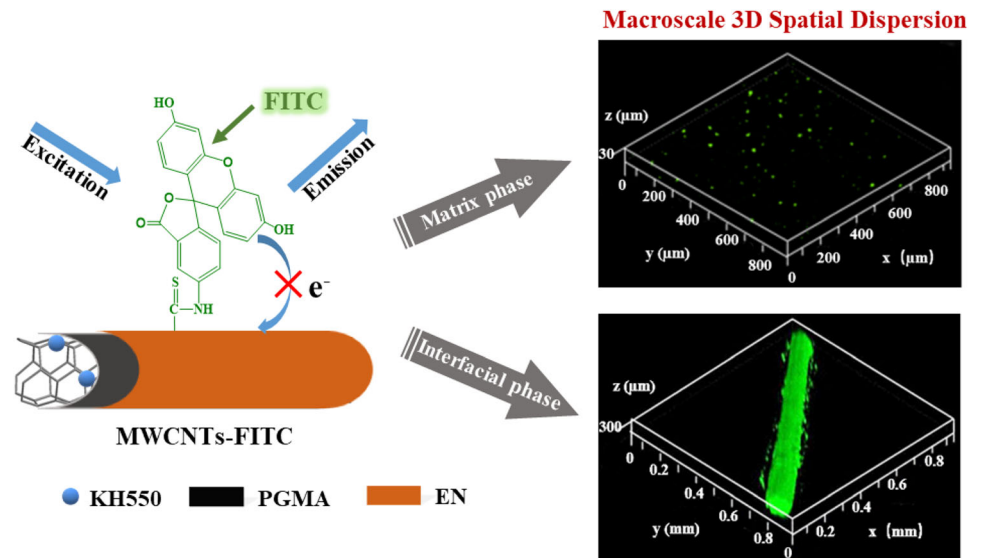
To effectively and simply characterize the macroscale dispersion of nanoparticles was vital for understanding the intrinsic connection between the properties and the structure of composites. In this study, fluorescent MWCNTs–FITC was successfully synthesized via grafting fluorescein isothiocyanate on the MWCNTs with protection of polyglycidyl methacrylate, which opened new avenues to in situ visualize the dispersion of carbon-based materials under confocal laser scanning microscopy. With the aid of this noninvasive method, macroscale 3D spatial dispersion of MWCNTs–FITC in both matrix and interfacial phases of quartz fibers/epoxy (QFs/EP) composites was quantitatively evaluated by integrating Morisita's index, particle spacing probability density theory, 2D fractal dimension and Einstein's Stokes theory. The results showed that the threshold for uniform dispersion of MWCNTs–FITC was 0.05 wt% due to the interactions of inter-particle van der Waals forces and physical entanglement. The highest particle spacing coefficient of MWCNTs–FITC ( $\bar{x}/s = 1.69$ ) was achieved curing at 25 °C, which indicated that MWCNTs–FITC was well dispersed in matrix, while for the dispersion in QFs/EP interface, the optimal curing temperature was 40 °C where the actual average diffusion distance ( $\bar{l}_m$ ) was as high as 6.3 μm. The purpose of the established quantification method in this study was to provide viable opportunities and inspirations for quantitatively evaluating the dispersion of nanoparticles.

Handling Editor: Andrea de Camargo.

Address correspondence to E-mail: jiaxl@mail.buct.edu.cn

<https://doi.org/10.1007/s10853-021-06350-x>

## GRAPHICAL ABSTRACT



## Introduction

Due to the excellent physical and chemical properties, such as high tensile and compressive strengths, great dielectric property, thermal and size stability and corrosion resistance, polymer-based nanocomposites filled with nanoparticles have been widely used in various advanced application fields like aerospace, marine, energy, construction and automobile industries [1–5]. As extensively recognized by both academic and engineering communities [6–10], the efficient achievement in all these excellent properties was strongly dependent on the dispersion state of nanoparticles in the polymer-based composites [11]. However, the actual dispersion of nanoparticles in the polymer matrix of composites was in a dynamic mode instead of a static status, which globally evolved during the whole processing stage of composites. For instance, at thermally induced curing process of polymer composites, the global sediment and aggregation of nanoparticles like carbon nanotubes (CNTs) always took place as a result of the combining functions of nanoparticle interactions, thermally driven microscale Brown motion and thermodynamic environment changing [12–14].

Thus, to effectively characterize the actual spatial dispersion of nanoparticles within the composites was very vital for understanding the structure–property relationships of composites and further controlling the optimal processing conditions to prepare the high-quality composites.

To date, the conventional observation methods for the dispersion of nanoparticles mainly included scanning electron microscopy (SEM) [15–17], transmission electron microscopy (TEM), three-dimensional (3D)-TEM tomography [10, 18], atomic-force microscopy (AFM) [12, 18, 19], element mapping [20–22], Raman mapping [23, 24] and contrast variation small-angle neutron scattering (CV-SANS) [25, 26]. In spite of obtaining a large amount of information on the dispersion of nanoparticles, these reported methods suffered from a degree of intrinsic limitations. Firstly, in most of these methods, the preparation of the testing sample was complicated and time-consuming, normally along with the sample damaging [27–29]. The quality of prepared sample was much affected by the professional level of technicians, which caused the frequent inconsistency of the final testing results. Secondly, the testing window was usually limited in a small domain area less than micrometers, which was only available for examining

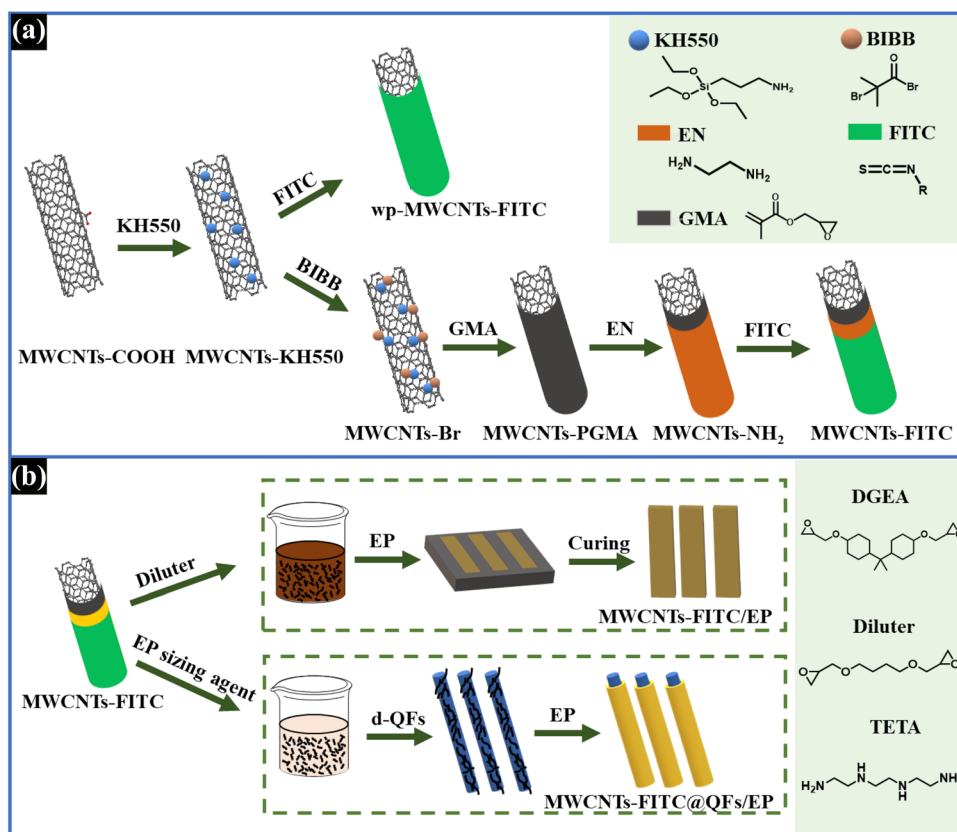
nanoscale dispersion of nanoparticles [28–30]. The acquired results from most of these methods were the only representative of the feature information from a two-dimensional (2D) view [27–30], other than reflecting the actual spatial dispersion of nanoparticles in the 3D space at a wide macroscale. Therefore, it was crucial to develop an alternative and simple methodology to realize precise and integrated evaluation for macroscale 3D spatial dispersion of nanoparticles in the composites.

Luckily, with the outstanding functions in visualizing internal structure of samples confocal laser scanning microscopy (CLSM) has become an attracting and powerful tool through combining fluorescence display technology with optical microscopy in biochemical research and material science in recent years [27–31]. On the premise of the stable light emission caused by fluorescent nanoparticles, CLSM could acquire the 3D visualization on samples in an ultrafast and noninvasive manner from a macroscale domain comprising hundreds of micrometers. Despite its advantages and convenience in characterizing dispersion of fluorescent nanoparticles, CLSM technology was hard to visualize the carbon-based nanoparticles (such as CNTs and graphene) in the composites even if the fluorescent dyes were directly loaded on their surfaces [32]. That's because, carbon materials with highly electrically conductive characteristics acted as electron acceptors of fluorescent dyes, leading to fluorescence quenching and invalidity of CLSM technology [33, 34]. To break this bottleneck, surface chemical-functionalization on carbon-based nanoparticles has been proposed to be effective in endowing them with stable fluorescence imaging capability by preventing direct contact between carbon material and fluorescein, along with enhancing their compatibility with polymer matrix simultaneously [35–37]. For instance, after surface modification with polystyrene and subsequent covalent labeling with benzo thioxanthene fluorescent dye, CNTs showed fluorescent feature in polystyrene-block-polyisoprene-block-polystyrene triblock copolymer rather than fluorescence quenching in their original state [38]. Nevertheless, the correlation between surface functionalization and fluorescent performance was inherently complex for nanoparticles. To the present, the fluorescence quenching mechanism of carbon-based nanoparticles was a relatively unexplored area of research. For this purpose, it would be quite helpful to look into the

light emission effect derived from the nanoscale interfacial interactions between carbon-based nanoparticles and surface functionalization layer.

Herein, in the present study, a facile approach was proposed to prepare fluorescent multi-walled CNTs (MWCNTs) by selecting fluorescein isothiocyanate (FITC) with good fluorescence stability and long fluorescence lifetime as an effective dye. As schematically shown in Fig. 1a, MWCNTs were firstly surface-grafted with polyglycidyl methacrylate (PGMA) via in situ surface-initiated atom transfer radical polymerization (ATRP) and then connected with ethylenediamine via ring-opening reaction to produce aminated MWCNTs. The final product MWCNTs–FITC were successfully obtained by covalent labeling of aminated MWCNTs with FITC via addition reaction. After characterizing their physicochemical features with Fourier transform infrared spectroscopy (FTIR), X-ray photoelectron spectroscopy (XPS), thermogravimetric analyzer (TGA), scanning electron microscopy (SEM) and transmission electron microscopy (TEM), the fluorescent performance and fluorescence emitting mechanism of MWCNTs–FITC were analyzed using ultraviolet–visible spectrophotometer (UV–Vis) and fluorescence spectrometer (FS). Then, the different samples of MWCNTs–FITC/epoxy (EP) composites and MWCNTs–FITC loaded quartz fibers (MWCNTs–FITC@QFs)/EP composites were prepared by changing MWCNTs–FITC content and curing temperature. Based on green fluorescent labeling observed in 3D CLSM images, the macroscale 3D spatial dispersion of MWCNTs–FITC in EP matrix phase was quantitatively evaluated using Morisita's index and particle spacing probability density theory. Moreover, the macroscale 3D spatial dispersion of MWCNTs–FITC in interfacial phase of MWCNTs–FITC@QFs/EP composites was also observed directly, and the corresponding diffusion of MWCNTs–FITC was examined using 2D fractal dimension and Einstein's Stokes theory. The reasonable mechanisms for the dispersion and diffusion of MWCNTs–FITC in MWCNTs–FITC@QFs/EP composites were proposed in concerning the affecting factor of curing temperature.

**Figure 1** Schematic for the preparation of (a) MWCNTs–FITC and wp-MWCNTs–FITC as well as (b) MWCNTs–FITC/EP and MWCNTs–FITC@QFs/EP.



## Experimental

### Materials

Carboxylated MWCNTs (MWCNTs–COOH, purity  $\geq 95\%$ , diameter 40–80 nm, length 10–20  $\mu\text{m}$ ) were purchased from Chengdu Organic Chemicals Co. Ltd. (China). Glycidyl methacrylate (GMA, purity  $\geq 97\%$ ) monomer, fluorescein isothiocyanate (FITC) and 2-bromo-2-methylpropionyl bromide (BIBB, purity  $\geq 98\%$ ) were obtained from Sigma-Aldrich Co. Silane coupling agent (KH550, purity  $\geq 97\%$ ) and cuprous bromide (CuBr) were obtained from Alfa-Aesar Co. *N, N, N', N', N''*-Pentamethyldiethylenetriamine (PMDETA) was obtained from TCI Shanghai Co. Ltd. (China). Ethylenediamine (EN) and triethylamine were both purchased from Beijing Tong Guang Fine Chemical Co. (China). Quartz fibers (QFs) coated with a modified-epoxy sizing agent (diameter  $\sim 20 \mu\text{m}$ ) were obtained from Shandong Glassfiber Co., Ltd. (China). The resin matrix, diglycidyl ether of bisphenol A (DGEBA) type epoxy resin (EP value, 0.51) and the diluter, 1,4-butanediol diglycidyl ether (EP value, 0.65–0.75) were purchased

from Shanghai Huayi resin Co. Ltd. (China). The curing agent, triethylenetetramine (TETA), was obtained from Lonza (Switzerland). All other chemicals and reagents were purchased from Beijing Chemical Works (China) and used directly.

### Preparation of fluorescent MWCNTs–FITC

The schematic for the preparation of FITC covalently labeled MWCNTs (MWCNTs–FITC) is shown in Fig. 1a. MWCNTs–COOH were strictly purified by washing with deionized water repeatedly to remove any possible impurities before use. In referring to our previous works [39, 40], MWCNTs–PGMA were prepared via in situ surface-initiated atom transfer radical polymerization (ATRP) through the three-step reactions of MWCNTs–COOH with KH550, BIBB and GMA in sequence. The prepared MWCNTs–PGMA were redispersed in a mixture of ethanol and EN by bath sonication for 30 min, and the subsequent reaction lasted for 24 h with magnetic stirring at 50  $^{\circ}\text{C}$ . Afterward, the aminated MWCNTs (MWCNTs–NH<sub>2</sub>) were successfully obtained by washing with absolute ethanol for several times and

drying in vacuum. The resulting MWCNTs–NH<sub>2</sub> were redispersed into the mixture of buffer solution (composed of NaCl, Na<sub>2</sub>CO<sub>3</sub>, NaHCO<sub>3</sub>) and deionized water by bath sonication for 30 min. Then, the FITC solution in dimethyl sulfoxide (DMSO) was dropwise added into the MWCNTs–NH<sub>2</sub> suspension under mechanical stirring. The mixture was reacted in the dark at room temperature for 8 h to avoid photo-bleaching. The final product, MWCNTs–FITC, were obtained by centrifugation, washing with deionized water for several times and drying in vacuum.

For comparison, MWCNTs–FITC without PGMA grafting (wp-MWCNTs–FITC) were prepared to explore the role of PGMA component in preventing fluorescence quenching of FITC grafted on electric-conductive carbon nanotubes. The schematic for the preparation of wp-MWCNTs–FITC is also shown in Fig. 1a. In detail, wp-MWCNTs–FITC were directly obtained by mixing FITC/DMSO solution into MWCNTs–KH550/DMSO suspension under mechanical stirring, followed by reacting in dark place at room temperature for 8 h and purifying in the end. The same conditions of centrifugation, washing with deionized water and drying in vacuum were also used in the purifying treatment.

### Composite preparation

The schematic for the preparation of MWCNTs–FITC/EP composites is shown in Fig. 1b. The MWCNTs–FITC were dispersed into diluter by sonication for 30 min to form suspension batch. Then, EP mixtures were obtained by mixing EP resin, TETA, diluter/MWCNTs–FITC batch. The MWCNTs–FITC/EP composites were prepared by pouring EP mixtures into molds and curing for 8 h. To guarantee the uniformity of the obtained MWCNTs–FITC/EP composites, the weight ratio of EP resin, diluter and curing agent was set as 60:40:22 to ensure a low system viscosity. The contents of MWCNTs–FITC in EP composites were adjusted to be 0.01, 0.05 or 0.10 wt% of the total weight of EP matrix. The curing temperature was set to be 25, 40, 80 °C, respectively.

The schematic for the preparation of MWCNTs–FITC loaded QFs (MWCNTs–FITC@QFs)/EP composites is also illustrated in Fig. 1b. Firstly, the QFs were desized in acetone for 48 h at 75 °C to remove the sizing agent and subsequently dried after repeated washing. Then DGEBA was dissolved in DMF at

weight ratio of 1:50 to fabricate the sizing agent. The MWCNTs–FITC were dispersed into the EP sizing agent at weight concentrations of 0.01, 0.05 and 0.10 wt%, respectively. Afterward, MWCNTs–FITC@QFs was obtained by immersing the desized QFs (*d*-QFs) into the mixture of MWCNTs–FITC and sizing agent for 12 h at room temperature, followed by drying at 80 °C for 2 h. Finally, MWCNTs–FITC@QFs/EP composites were prepared by coating the mixed EP on the fiber bundle and soaking it thoroughly, then curing in a stainless-steel mold for 8 h at different temperatures of 25, 40 and 80 °C, accordingly.

### Dispersion index

#### *Morisita's index*

The concept of the overall dispersion degree was proposed by Masaaki Morisita and. Morisita's Index was applied to the application of dispersion and distribution models, which was defined as Eq. (1) [41, 42].

$$I = Q \frac{\sum_i m_i(m_i - 1)}{M(M - 1)} \quad (1)$$

where  $Q$  is the total section number,  $M$  is the total inclusion number and  $m_i$  is the inclusion number in section  $i$ . It is smaller than 1 for random and dispersed system while larger than 1 for agglomerated system.

#### *Particle spacing probability density theory*

Particle spacing probability density was used to evaluate the dispersion of MWCNTs–FITC quantitatively (Supplementary Information displays the details). In the actual statistical calculation, the average particle spacing was  $\bar{x}$ , which could be calculated from Eq. (2) [42, 43]. Also, the standard deviation was  $s$ , and its calculation was based on Eq. (3) [42, 43].

$$\bar{x} = \frac{\sum_i x_i}{N} \quad (2)$$

$$s = \sqrt{\frac{\sum_i (x_i - \bar{x})^2}{N - 1}} \quad (3)$$

#### *Nanoparticle diffusion theory*

Based on the theory of single-particle tracer (SPT), the diffusion mechanism of nanoparticles was studied.

The relationship between the particle diffusion coefficient and the mean square displacement was expressed as Eq. (4) [44, 45].

$$\overline{l_t^2} = 2D_{NP}\Delta t \quad (4)$$

where  $D_{NP}$  is the diffusion coefficient of the particles,  $\Delta t$  is the observation time interval in the experiment, and  $\overline{l_t^2}$  is the mean square displacement referring to the displacement distance of the particles in the  $\Delta t$  time.  $D_{NP}$  could be derived from resistance formula of Einstein's Stokes theory as Eq. (5) [45–47].

$$D_{NP} = \frac{kT}{3\pi\eta\phi} \quad (5)$$

where  $k$  is the Boltzmann constant,  $T$  is the absolute temperature,  $\eta$  is the viscosity of the fluid (containing particles), and  $\phi$  is the diameter of the particles. The actual average diffusion distance was  $\overline{l_m}$ , which could be calculated from Eq. (6).

$$\overline{l_m} = \frac{\sum_i l_i}{N} \quad (6)$$

## Characterizations

Changes of the functional groups on the surface of MWCNTs were detected by Fourier transform infrared spectroscope (FTIR, Nexus670, Nicolet). Element analysis on different MWCNTs prepared at various stages was conducted on X-ray photoelectron spectroscopy (XPS, ESCALAB 250, Thermo Scientific) using mono chromicized Al K $\alpha$  X-ray source at a constant analyzer. Thermal stability was measured on thermogravimetric analyzer (TGA, Q500, TA) at a heating rate of 10 °C/min from 30 to 600 °C under nitrogen atmosphere. Morphological observations were performed on scanning electron microscope (SEM, S4700, Hitachi) and transmission electron microscope (TEM, JEM100CX, Leica). Before SEM examination, samples were coated with a thin layer of a gold alloy. The elements in selected regions were analyzed under energy disperse X-ray spectroscopy (EDS, ESCALAB 250, Thermo Scientific). Typical tapping-mode atomic-force microscope (AFM) measurements were performed using Dimension Fast Scan from Bruker. The fluorescent properties of MWCNTs–FITC were detected by using ultraviolet-visible spectrophotometer (UV-Vis, UV-3600, Shimadzu), fluorescence spectrometer (FS, F-7000, Techcomp) and confocal laser scanning microscope

(CLSM, SP8, Leica). Before CLSM observation, samples were prepared by dispersing MWCNTs–FITC into ethanol at a concentration of  $2 \times 10^{-5}$  g/mL. The average size and size distribution of MWCNTs–FITC were calculated with contrast-treated CLSM images by using ImageJ software to measure at least 1000 particles, as well as they were directly tested with dynamic light scattering (DLS, ZEN1600, Zetasizer Nano). The area size ( $A$ ) of MWCNTs–FITC aggregate and the maximum length ( $L$ ) of aggregate area were also determined from contrast-treated CLSM images using ImageJ. The gel time of EP matrix was determined using around 100 mg of sample according to ASTM 2471 [48].

## Results and discussion

### The analysis of MWCNTs–FITC

The different MWCNTs prepared at various stages were characterized by FTIR, XPS, TGA, SEM and TEM. In referring to our previous works [39, 40], MWCNTs–PGMA were prepared via ATRP through the three-step reactions of MWCNTs–COOH with KH550, BIBB and GMA in a proper sequence. As shown in Fig. 2a, the resulting MWCNTs–PGMA clearly displayed characteristic adsorption of C=O stretching vibrations at 1629 and 1728  $\text{cm}^{-1}$ , which apparently came from carboxyl and ester groups contained in GMA component, respectively. Additionally, in the FTIR spectrum of MWCNTs–PGMA, the adsorption peaks at 1149 and 1256  $\text{cm}^{-1}$  were originated from the asymmetrical and symmetrical stretching vibrations of  $-\text{CH}_3$  group in GMA component, respectively, as well as the absorption peak at 906  $\text{cm}^{-1}$  was also ascribed to epoxide groups in GMA component [39, 49]. Compared to MWCNTs–PGMA, a new peak at 1553  $\text{cm}^{-1}$  appeared in the spectrum of MWCNTs–NH $_2$ , which corresponded to the  $-\text{N}-\text{H}$  stretching vibration. After the reactions between epoxide groups in GMA and  $-\text{NH}_2$  groups in ethylenediamine, the absorption peak of epoxide groups at 906  $\text{cm}^{-1}$  in GMA disappeared in the spectrum of MWCNTs–NH $_2$ . Together with the presence of characteristic peak for C=S group at 1465  $\text{cm}^{-1}$ , the chemical structure features of FITC were obviously detected in MWCNTs–FITC.

Also, these chemical changes on different MWCNTs were confirmed from XPS testing, as

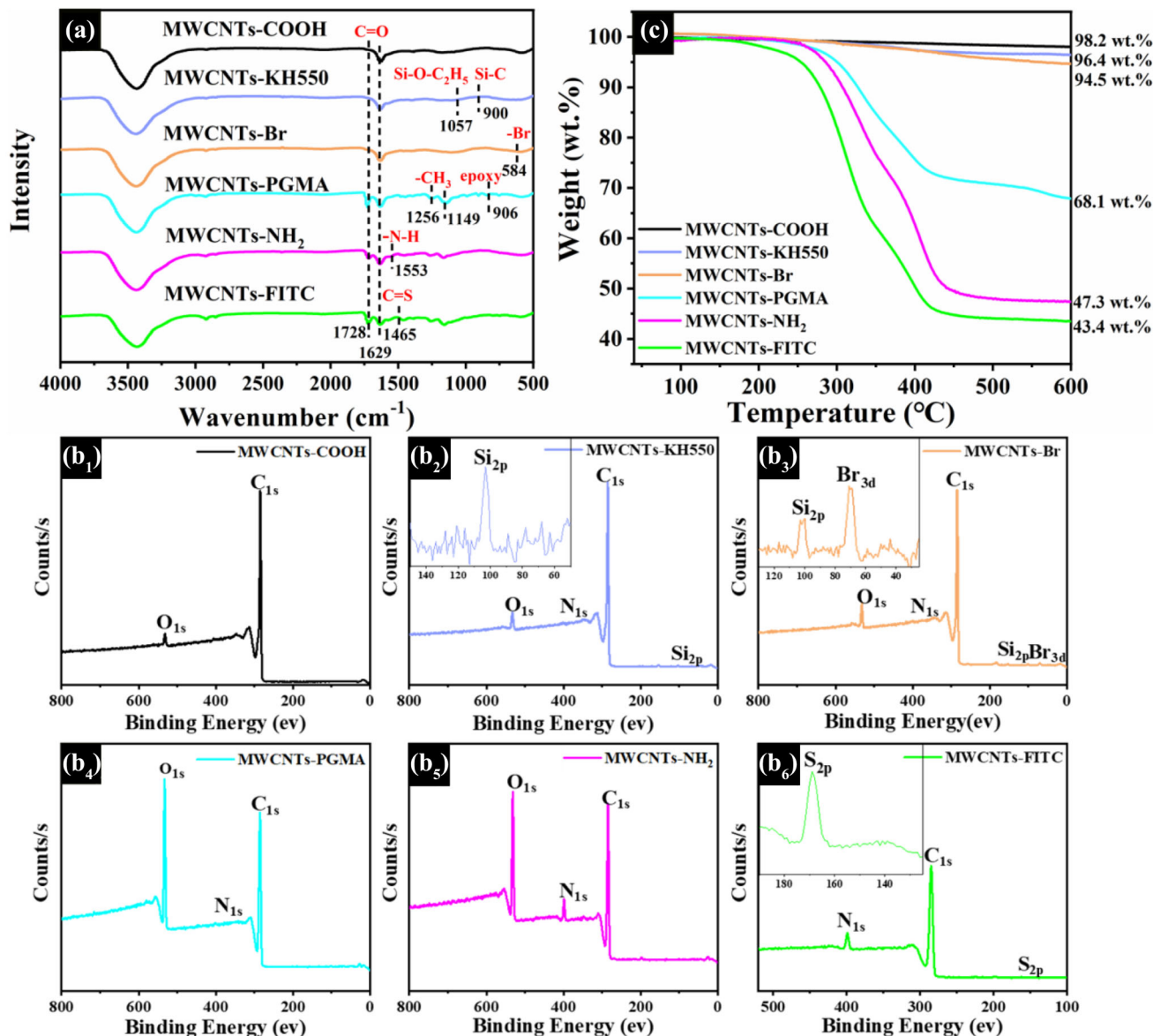


**Figure 2** a FTIR, b XPS spectra and c TGA curves of MWCNTs-COOH, MWCNTs-KH550, MWCNTs-Br, MWCNTs-PGMA, MWCNTs-NH<sub>2</sub> and MWCNTs-FITC.

shown in Fig. 2b, and the atom contents of different elements in these MWCNTs are listed in Table S1. The characteristic peaks of C<sub>1s</sub> and O<sub>1s</sub> were observed at 285.2 and 533.1 eV in the XPS spectrum of MWCNTs-COOH (Fig. 2b<sub>1</sub>), respectively. After grafting KH550, two new peaks appeared at 400.2 and 102.4 eV in the spectrum of MWCNTs-KH550, respectively, which were attributed to the N<sub>1s</sub> and Si<sub>2p</sub> in KH550 [50, 51]. The corresponding atomic contents of element N and Si were 0.32 and 0.63%. Compared to MWCNTs-KH550, an additional characteristic peak at 68 eV in the spectrum of MWCNTs-

Br corresponded to the Br<sub>3d</sub> and the atomic content of element Br was 0.52%. It was seen that the intensity in the characteristic peak of O<sub>1s</sub> at 533.1 eV was increased a lot in XPS spectrum of MWCNTs-PGMA and the content of element O was increased to 10.04%, which was apparently due to the introduction of epoxide groups after comparing with the spectrum of MWCNTs-Br (Fig. 2b<sub>4</sub>). The characteristic peak of N<sub>1s</sub> at 400.2 eV was also intensified as observed in the XPS spectrum of MWCNTs-NH<sub>2</sub> along with the atomic content of element N increasing to 5.84% from 0.56% for MWCNTs-PGMA,

indicating the successful introduction of the  $-\text{NH}_2$  groups (Fig. 2 b<sub>5</sub>). More importantly, the unique peak of  $\text{S}_{2\text{p}}$  at 165.2 eV from isothiocyanate group in FITC was found in the XPS spectrum of MWCNTs–FITC (Fig. 2b<sub>6</sub>). Thus, the FTIR and XPS data proved the successful grafting of FITC onto MWCNTs.

Then, the thermal stabilities of different MWCNTs at various preparation stages were measured using TGA. As shown in Fig. 2c, compared with the value of  $\sim 1.8$  wt% for MWCNTs–COOH, the weight loss at 600 °C increased gradually in values of  $\sim 3.6$ ,  $\sim 5.5$ ,  $\sim 31.9$ ,  $\sim 52.7$  and  $\sim 56.6$  wt% for MWCNTs–KH550, MWCNTs–Br, MWCNTs–PGMA, MWCNTs– $\text{NH}_2$  and MWCNTs–FITC, respectively, verifying the success in each step of modification. Specifically, the three samples of MWCNTs–PGMA, MWCNTs– $\text{NH}_2$  and MWCNTs–FITC showed the significant weight loss over  $\sim 300$  °C, as a result of the thermal decomposition of the grafted organic components. The weight content of FITC in MWCNTs could be calculated using the equation of  $f_{\text{MWCNTs-FITC}} - f_{\text{MWCNTs-NH}_2} = (1 - f_{\text{MWCNTs-FITC}}) \times x$ , where  $f_{\text{MWCNTs-FITC}}$  and  $f_{\text{MWCNTs-NH}_2}$  meant the weight loss percentage of MWCNTs–FITC and MWCNTs– $\text{NH}_2$ , respectively, and  $x$  denoted the weight content of FITC in MWCNTs–FITC. Finally, the weight content of FITC in MWCNTs–FITC was calculated to be  $\sim 8.9$  wt%. Among them, most of the FITC and MWCNTs were covalently connected, and there was also a few non-covalent bonding that could not be ignored [52].

Additionally, the morphologies of MWCNTs–COOH, MWCNTs–FITC and wp-MWCNTs–FITC were observed by both SEM and TEM. As shown in Fig. 3a<sub>1</sub>, the typical hollow and rod-like structure was seen for MWCNTs–COOH. Different from the smooth surface of MWCNTs–COOH, MWCNTs–FITC looked rough with a coating shell on the surface. The shell was distributed uniformly at a thickness of  $\sim 5.7$  nm from the wrapped edge (Fig. 3a<sub>2</sub>, b<sub>2</sub>), confirming the successful grafting of PGMA and FITC onto MWCNTs. As expected, wp-MWCNTs–FITC showed the similar rough surface with coating shells, but possessed a thinner shell thickness of  $\sim 1.5$  nm compared with MWCNTs–FITC, as shown in Fig. 3a<sub>3</sub>. This observed morphology was similar to the reported results in the literature [53] and our previous works [39, 40]. Moreover, it was found from the SEM image in Fig. 3b<sub>1</sub> that MWCNTs–COOH

showed a sort of aggregated state. In contrast, MWCNTs–FITC and wp-MWCNTs–FITC seemed to exist in a uniform state due to their better dispersion capabilities in ethanol.

The absorption, excitation and emission performance of FITC, MWCNTs– $\text{NH}_2$  and MWCNTs–FITC were evaluated with UV–Vis and FS. It could be seen from Fig. 4a<sub>1</sub>–a<sub>3</sub> that the maximum absorption, excitation and emission for FITC were at the peak wavelengths of 478, 487 and 516 nm, respectively. This was the typical green fluorescent characteristics of FITC as reported in the literature [54]. And as expected, there was no any peak in the absorption, excitation and emission spectra of MWCNTs– $\text{NH}_2$  (Fig. 4b<sub>1</sub>–b<sub>3</sub>). It was known that MWCNTs normally manifested the quenching effect on the fluorescent light due to the high electrical conductivity of carbon structure [49]. Differently, MWCNTs–FITC showed the strong absorption, excitation and emission abilities at peak wavelengths of 500, 490 and 519 nm, accordingly, proving the success in grafting FITC onto MWCNTs– $\text{NH}_2$ . Noticeably, the wavelength values of absorption, excitation and emission peaks in the spectra of MWCNTs–FITC were higher than those in the spectra of FITC. The phenomenon should be attributed to a redshift in the peak wavelength due to the existence of the  $-\text{NH}_2$  group in the grafting layers of MWCNTs–FITC [54, 55]. The above results demonstrated that it was effective to protect FITC from the direct contact with MWCNTs by grafting PGMA onto MWCNTs, which guaranteed the tracer role of MWCNTs–FITC with displaying the fluorescent feature.

The direct fluorescent feature of wp-MWCNTs–FITC and MWCNTs–FITC was observed by CLSM. Clearly, there was almost no fluorescence observed for wp-MWCNTs–FITC in 2D CLSM image (Fig. 5a) and 3D CLSM image (Fig. S3a<sub>1</sub>), even though FITC with green fluorescence had been grafted onto them. But it could be seen that MWCNTs–FITC emitted strong green fluorescent light as shown in 2D CLSM image of Fig. 5b. This confirmed that wp-MWCNTs–FITC displayed the quenching morphology without fluorescence due to the high electrical conductivity of carbon structure in MWCNTs as well as the possible existence of the residual catalyst metals used in preparing MWCNTs [49, 56–58]. The microscale structure and distribution state of MWCNTs–FITC in a 3D large-scale volume could be clearly characterized from their 3D CLSM images (Fig. S3a<sub>2</sub>). The



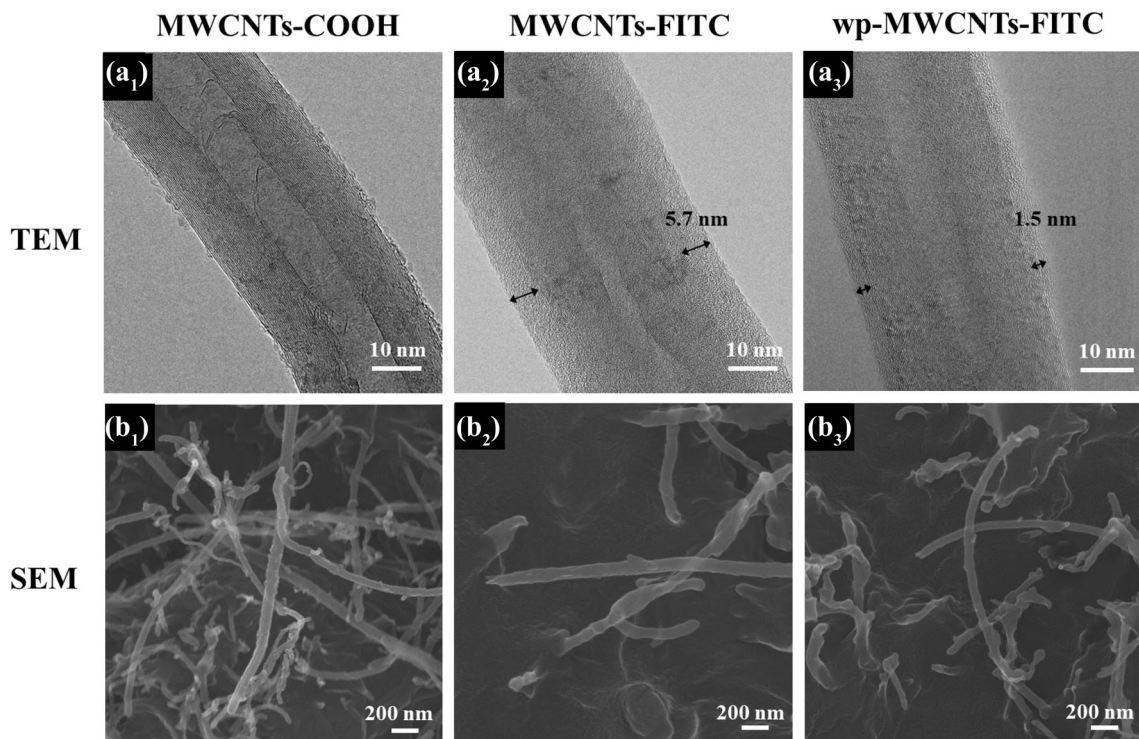


Figure 3 TEM and SEM images of a<sub>1</sub>, b<sub>1</sub> MWCNTs–COOH, a<sub>2</sub>, b<sub>2</sub> MWCNTs–FITC and a<sub>3</sub>, b<sub>3</sub> wp- MWCNTs–FITC.

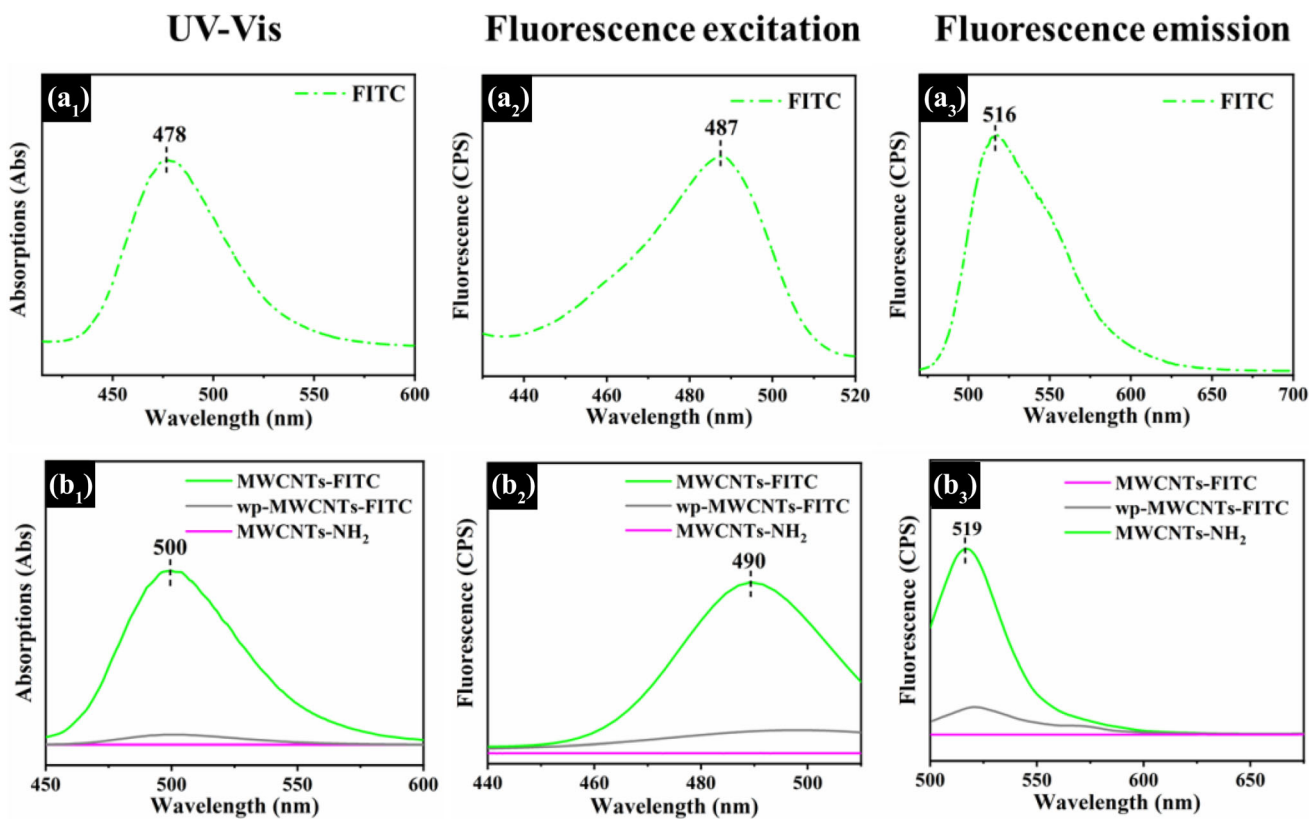
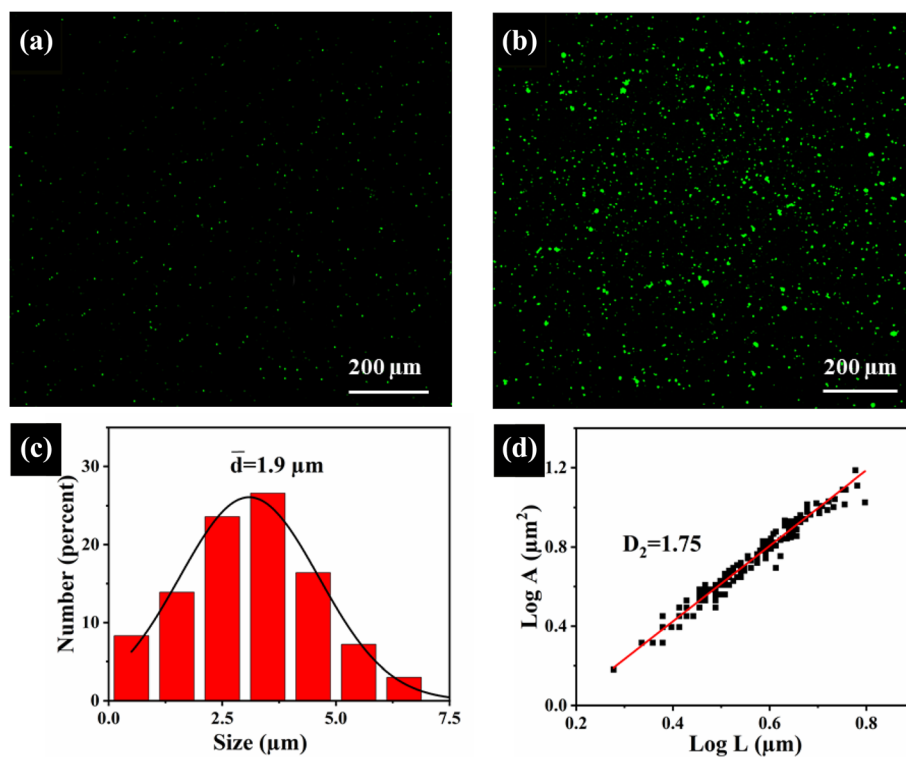


Figure 4 a<sub>1</sub>, b<sub>1</sub> UV–Vis, a<sub>2</sub>, b<sub>2</sub> fluorescence excitation and a<sub>3</sub>, b<sub>3</sub> fluorescence emission spectra of FITC, MWCNTs–NH<sub>2</sub>, wp-MWCNTs–FITC and MWCNTs–FITC.

**Figure 5** **a** 2D CLSM images of (a) wp-MWCNTs–FITC and **b** MWCNTs–FITC, as well as (c) particle size distribution histogram of MWCNTs–FITC by practical statistics, and (d)  $\log A$  versus  $\log L$  curve of MWCNTs–FITC.



fluorescence imaging provided a direct way to observe macroscale special dispersion of MWCNTs from the 3D directions. In order to directly measure the particle size of MWCNTs–FITC, their 2D CLSM image (Fig. 5b) was binarized using the software ImageJ, and the exact boundary contours of all MWCNTs–FITC were extracted as presented in Fig. S3b<sub>1</sub>. Then, the particle size of MWCNTs–FITC could be directly measured, and the obtained particle size distribution histogram based on statistical results is shown in Fig. 5c. It was found that particle size of MWCNTs–FITC was close to the normal distribution. And the average particle size of MWCNTs–FITC was  $\sim 1.9 \mu\text{m}$ , which was much close to the value of  $\sim 1.1 \mu\text{m}$  measured by using the technique of DLS as an auxiliary characterization (Fig. S3b<sub>2</sub>). Notedly, the measured size value implied that the uniformly dispersed MWCNTs–FITC were not the individual MWCNTs, but the MWCNTs aggregates. This finding was due to the intrinsic interactions between CNTs-based nanomaterials, such as inter-particle van der Waals forces, physical entanglement and physical stacking, which was consistent with the reported results in the literatures [59, 60] and our previous works [39, 40]. Thus, to quantitatively describe the microstructure feature of MWCNTs–FITC, the 2D

fractal dimension ( $D_2$ ) was applied (Fig. 5d) [61, 62].  $D_2$  was obtained by the slope measured through the relationship between areas ( $A$ ) and maximum lengths ( $L$ ) by the definition of  $A \propto L^{D_2}$ , where  $A$  and  $L$  are the area size of MWCNTs–FITC aggregates and the maximum length of such area.  $\log A$  was plotted versus  $\log L$  as shown in Fig. 5d. The fractal dimension was an evaluation of the space filling efficiency of the aggregate structures, and the  $D_2$  value of 2D objects with regular circular shape was 2 theoretically. Lower  $D_2$  value meant the formation of irregular-shaped aggregates with loose structure, corresponding to larger area proportion of aggregates in unit area. The  $D_2$  value of MWCNTs–FITC was calculated to be 1.75, indicating that the aggregated structure of MWCNTs–FITC was relatively dense. The dense structure of MWCNTs–FITC aggregates was favorable for their dispersion in EP matrix in the following study.

### Fluorescence emitting mechanism of MWCNTs–FITC

According to the literatures [33, 38, 57], the carbon-based nanostructures like CNTs would result in the big possibility in fluorescence quenching due to the high electrical conductivity of carbon materials as

well as the possible existence of the residual catalyst metals used in preparing the nanostructures. In considering all the above results, the prepared MWCNTs–FITC had shown different surface morphology and chemical feature from initial MWCNTs–COOH, which evoked our keen interest in studying its fluorescence emitting mechanism upon the grafting layer on MWCNTs–FITC. For comparison, MWCNTs–FITC without PGMA in the grafting layer (wp-MWCNTs–FITC) were prepared. As observed from TEM and SEM images in Fig. 3a<sub>2</sub>–a<sub>3</sub>, b<sub>2</sub>–b<sub>3</sub>, both wp-MWCNTs–FITC and MWCNTs–FITC showed the similar rough surfaces with coating shells. As expected, wp-MWCNTs–FITC possessed a thinner shell thickness of  $\sim 1.5$  nm compared with MWCNTs–FITC. Furthermore, the differences in the excitation and emission performance of both wp-MWCNTs–FITC and MWCNTs–FITC were examined with UV–Vis and FS. Compared with MWCNTs–FITC, the absorption peak of wp-MWCNTs–FITC decreased to a very weak level as shown in Fig. 4b<sub>1</sub>. As seen in Fig. 4b<sub>2</sub>, b<sub>3</sub>, completely different from the strong excitation and emission abilities with high peak intensities for MWCNTs–FITC, the excitation and emission peaks were detected at rather low intensities in the spectra of wp-MWCNTs–FITC. The results of UV–Vis and FS measurements manifested the quenching phenomenon of fluorescent light on wp-MWCNTs–FITC, which was consistent with the reported results for CNTs or GO [33, 62]. In addition, such phenomenon could be directly observed from 2D CLSM image as shown in Fig. 5a, b. It was found that wp-MWCNTs–FITC clearly displayed the quenching morphology almost without the green fluorescence as observed for MWCNTs–FITC. These findings suggested that the PGMA component in the grafting layer played a decisive role in endowing the fluorescent feature to MWCNTs.

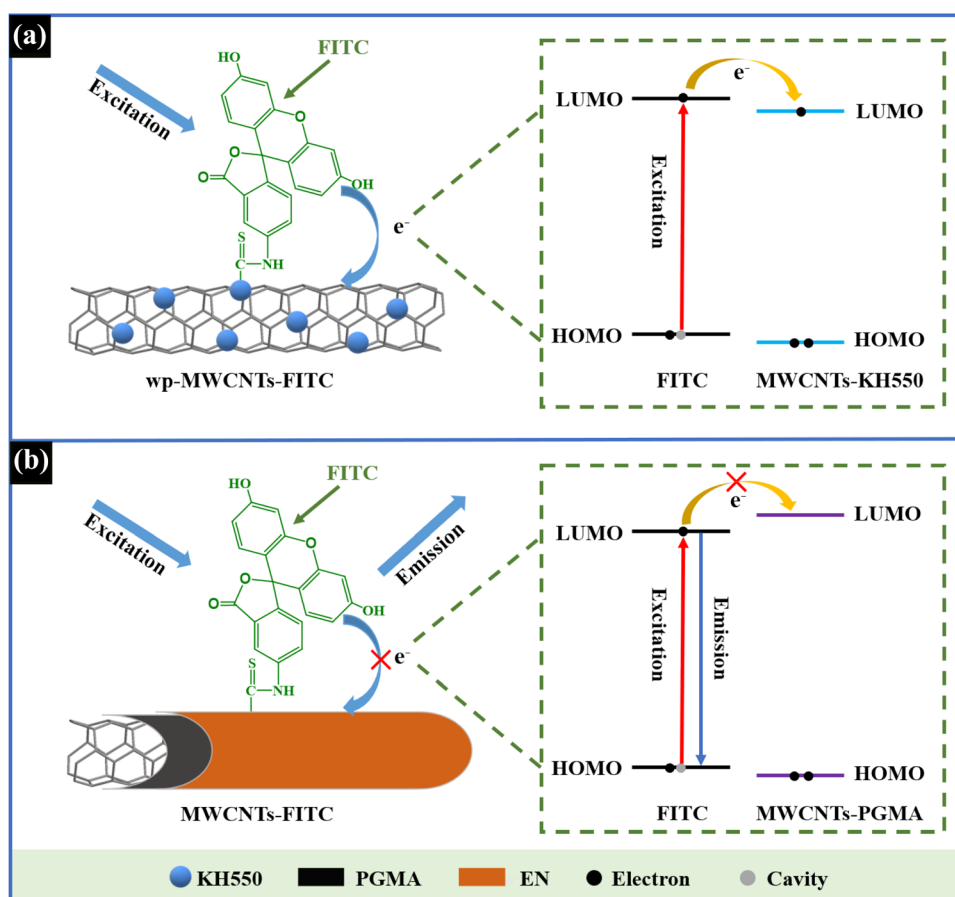
Based on the above findings, the mechanisms for fluorescence quenching of wp-MWCNTs–FITC and fluorescence emitting of MWCNTs–FITC were proposed as presented in Fig. 6. Normally, the fluorescence quenching or emitting was primarily dependent on the charge transfer path inside the materials. Under the action of excitation light, the electrons inside the fluorescent dyes were excited and transition from the highest occupied molecular orbital (HOMO) to the lowest unoccupied molecular orbital (LUMO). When the excited electrons underwent a radiative transition from the LUMO to HOMO

and returned to the ground state, the excess energy was released in the form of a photon, and the fluorescent light was synchronously emitted by the materials [63]. In the present study, since the fluorescent dye FITC was introduced onto the surfaces of MWCNTs, FITC would act as a donor of electrons [57, 64]. In the case of wp-MWCNTs–FITC as shown in Fig. 6a, the electrons in FITC were initially excited by excitation light and transferred from HOMO to LUMO. However, the LUMO energy level of MWCNTs–KH550 located between HOMO and LUMO energy levels of FITC [64, 65]. Due to the high electrical conductivity of regular hexagon carbon nanostructure in walls of MWCNTs, MWCNTs–KH550 inside wp-MWCNTs–FITC should as the acceptor of electrons. Thus, before undergoing a radiative transition, the excited electrons from FITC were more inclined to transfer to the LUMO of the acceptor MWCNTs–KH550 instead of returning to the HOMO of FITC. Subsequently, these electrons were conductive away by hexagon carbon nanostructure of MWCNTs, resulting in fluorescence quenching on wp-MWCNTs–FITC. In contrast, after coating the insulator PGMA onto MWCNTs–KH550 as shown in Fig. 6b, the LUMO energy level of MWCNTs–PGMA was increased, since the LUMO energy level of PGMA was higher than that of FITC [66]. At this condition, the excited electrons could not transfer from LUMO of FITC to LUMO of MWCNTs–PGMA, but return back to HOMO of FITC along with emitting the fluorescent light. This was the exact mechanism for decisive role of the PGMA component in endowing the fluorescent feature to MWCNTs.

### Observation of MWCNTs–FITC in EP

Based on the fluorescent feature of MWCNTs–FITC, 3D CLSM images were firstly taken to evaluate the variation of macroscale spatial dispersion state and particle size of MWCNTs–FITC dispersed in the EP resin phase before and after curing. As shown in Fig. 7, it was difficult for MWCNTs–FITC to achieve monodispersed morphology in the EP resin, but in a state of aggregates, also due to the interactions of inter-particle van der Waals forces, physical entanglement, physical stacking, etc. MWCNTs–FITC aggregates with bigger size exhibited much stronger green fluorescent light with bigger fluorescent area in 3D space of EP resin. It could be seen in both cases before and after curing that the size and number of

**Figure 6** Mechanisms for (a) fluorescence quenching of wp-MWCNTs–FITC and (b) fluorescence emitting of MWCNTs–FITC.



aggregates increased with MWCNTs–FITC content from Fig. 7a<sub>1</sub>–a<sub>3</sub>, c<sub>1</sub>–c<sub>3</sub>. In detail, when the MWCNTs–FITC content was as high as 0.10 wt%, the size and number of aggregates increased sharply. What's more, such phenomena became more obvious after the EP resin was cured. This implied that, as the curing process progressed, the evolutions in the EP viscosity and the thermodynamic environment around MWCNTs–FITC might cause the secondary aggregation of MWCNTs–FITC. In order to characterize the dispersion state of MWCNTs–FITC in the EP resin phase quantitatively, the Morisita's index ( $I$ ) was used here and the calculated results are listed in Table 1. Normally, the closer the  $I$  value was to 1, the better the dispersion of particles [41, 42]. It was found that the  $I$  value increased with MWCNTs–FITC content in both cases before and after curing, which was consistent with the detected results from CLSM images. At the same content of MWCNTs–FITC, the  $I$  value for the sample after curing was higher than that for the sample before curing, reflecting the worsening in the dispersion of MWCNTs–FITC during the

curing process. Besides, another method, the particle spacing probability density theory, was chosen to further characterize and compare the dispersion state of MWCNTs–FITC in the EP resin phase before and after curing. Firstly, the 3D CLSM images were layered and contrasted to obtain a series of 2D images. Secondly, the software ImageJ was used to binarize the 2D images and extract the exact boundary contour of all MWCNTs–FITC aggregates in the whole image. Finally, the spacing  $\bar{x}$  between MWCNTs–FITC could be directly measured from the binarized 2D images and the statistical results are shown in Fig. 7b<sub>1</sub>–b<sub>3</sub>, d<sub>1</sub>–d<sub>3</sub>. Usually, the  $\bar{x}/s$  value could be considered to be proportional to the dispersion coefficient of particles, which thus was a quantitative description on the dispersion state of particles in the dispersion system. The larger the  $\bar{x}/s$  value, the more uniform the dispersion. Logically, as listed in Table 1, the  $\bar{x}$  and  $\bar{x}/s$  values decreased with MWCNTs–FITC content in both cases before and after curing, indicating that the dispersion of MWCNTs–FITC was gradually worsened. It illustrated that the content of

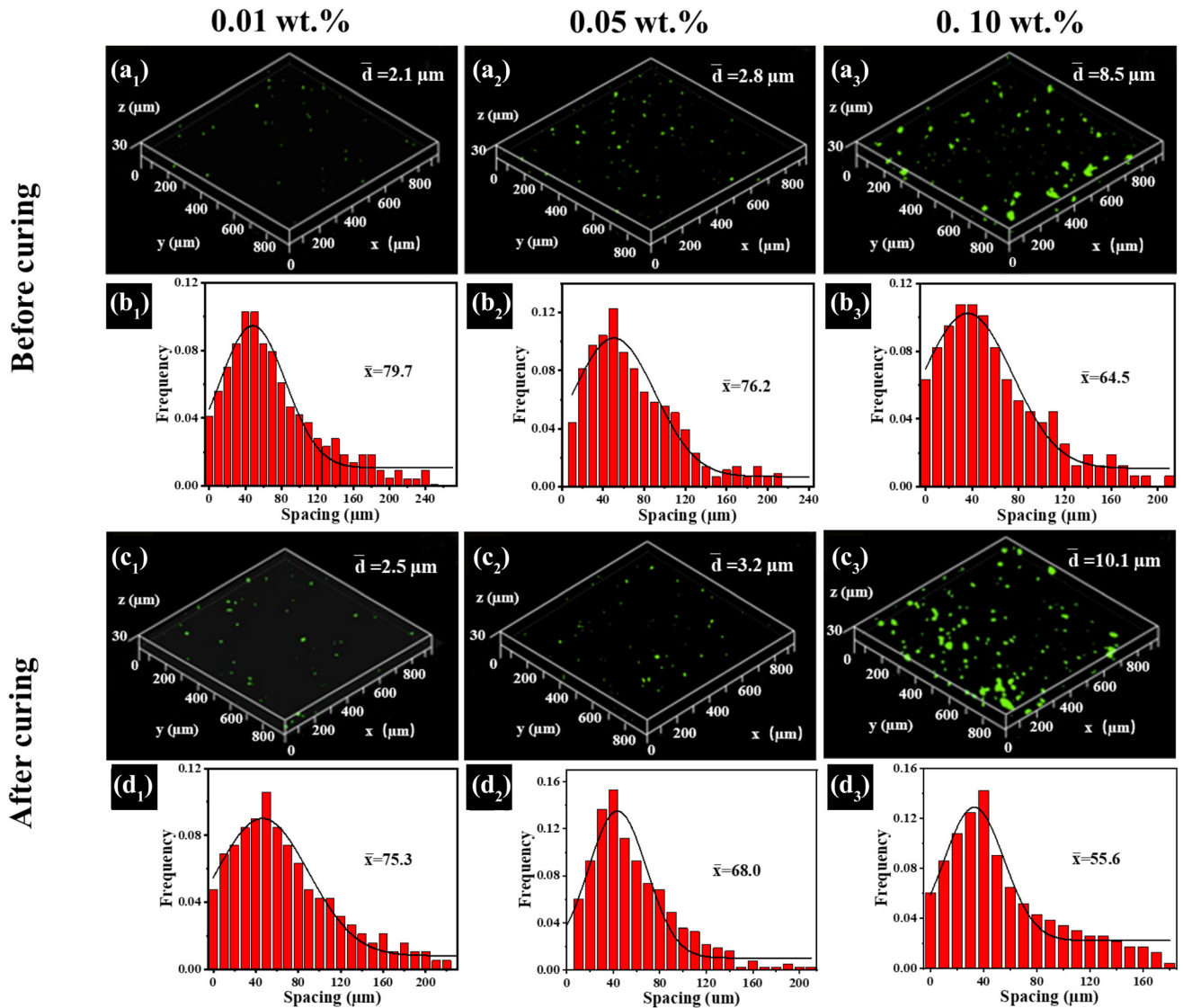


**Figure 7** a<sub>1</sub>–a<sub>3</sub>, c<sub>1</sub>–c<sub>3</sub> 3D CLSM images and b<sub>1</sub>–b<sub>3</sub>, d<sub>1</sub>–d<sub>3</sub> particle spacing distribution of MWCNTs–FITC in EP at contents of 0.01, 0.05 and 0.10 wt% before and after curing.

MWCNTs was detrimental to the dispersion degree in the dispersion system as reported in the literatures [42, 43]. Moreover, the  $\bar{x}$  and  $\bar{x}/s$  values for samples after curing were apparently lower than those for samples before curing when MWCNTs–FITC were controlled in the same content. This comparison demonstrated that the dispersion uniformity and stability of MWCNTs were greatly affected by the global evolutions in the microstructure of EP resin and in the thermodynamic environment around MWCNTs–FITC along with the curing process.

As widely reported in the literatures [67, 68], the temperature was the critical factor affecting the evolutions in the thermodynamic environment and

microstructure of thermosetting polymers like EP resin during the curing process. It was possible that the fluorescence performance of MWCNTs–FITC would disappear at the high temperature over 100 °C due to the cleavage of chemical bonds linking FITC and MWCNTs [69, 70]. Here, EP system with 0.05 wt% content of MWCNTs–FITC was cured at 25, 40 and 80 °C, respectively, and the corresponding 3D CLSM images of MWCNTs–FITC are shown in Fig. 8a<sub>1</sub>–a<sub>3</sub>. Also as predicted, the size and number of MWCNTs–FITC aggregates increased with the curing temperature. And all these values were higher than those for the case before curing. The Morisita’s index (*I*) and particle spacing probability density theory

were used again. The particle spacing distribution of MWCNTs–FITC in EP is shown in Fig. 8b<sub>1</sub>–b<sub>3</sub> and all calculated results are listed in Table 2. With the curing temperature increasing, the  $I$  value increased a

**Table 1** Morisita's index, average particle distance and  $\bar{x}/s$  value for MWCNTs–FITC in EP at contents of 0.01, 0.05 and 0.10 wt.% before and after curing

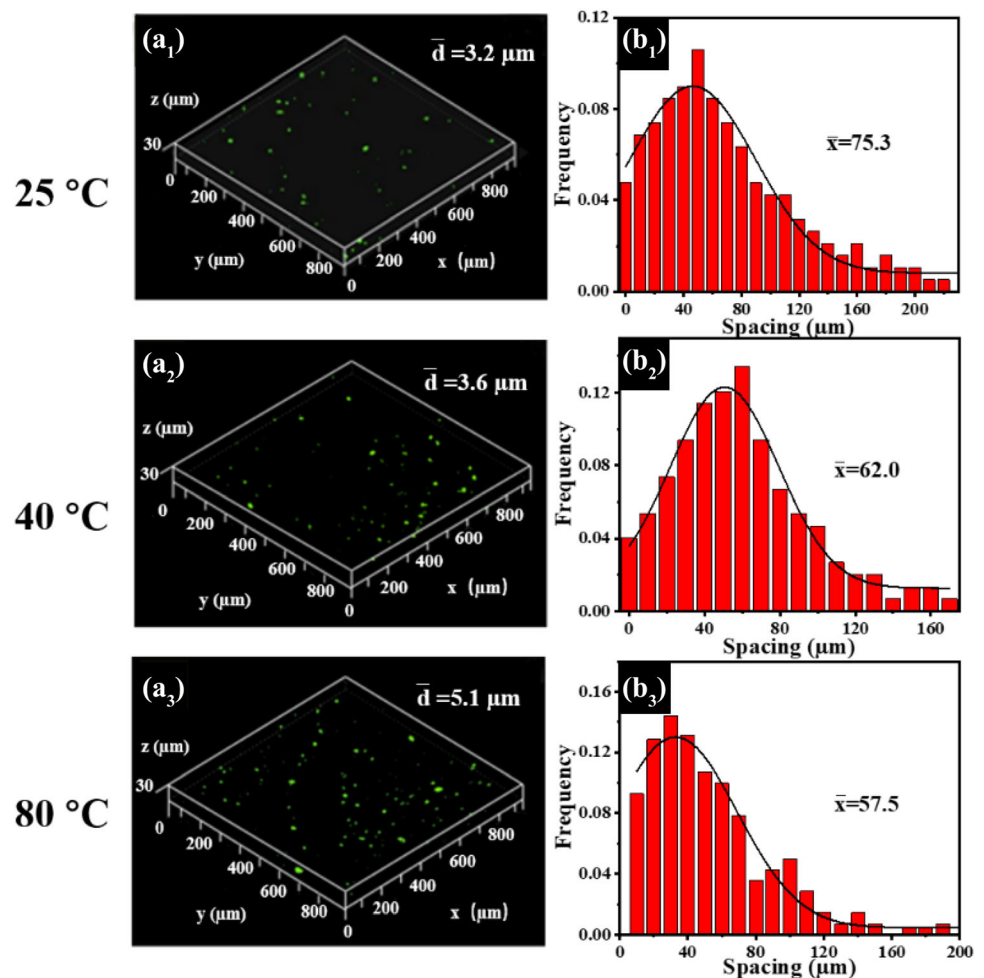
Sample	Index $I$	$\bar{x}$ ( $\mu\text{m}$ )	$s$ ( $\mu\text{m}$ )	$\bar{x}/s$
<i>0.01 wt%</i>				
Before	1.03	79.7	46.1	1.73
After	1.05	75.3	44.6	1.69
<i>0.05 wt%</i>				
Before	1.00	73.2	43.1	1.70
After	1.01	68.3	41.4	1.65
<i>0.10 wt%</i>				
Before	1.03	64.5	42.6	1.51
After	1.07	55.6	39.2	1.42

bit, while the  $\bar{x}$  and  $\bar{x}/s$  values decreased clearly. These verified that the dispersion uniformity and stability of MWCNTs–FITC in EP were worsened with the curing temperature as observed in Fig. 8. In fact, the temperature gradient always existed from the outside to the inside in the polymer/particle mixing system when it was thermally heated from the outside. And with the curing temperature increasing, this temperature gradient would become sharper inside the system. The thermodynamic environment

**Table 2** Morisita's index, average particle distance and  $\bar{x}/s$  value for MWCNTs–FITC dispersed in EP after curing at 25, 40 and 80 °C

Sample (0.05 wt%) (°C)	Index $I$	$\bar{x}$ ( $\mu\text{m}$ )	$s$ ( $\mu\text{m}$ )	$\bar{x}/s$
25	1.00	75.3	44.6	1.69
40	1.01	62.0	37.5	1.65
80	1.02	57.5	38.7	1.49

**Figure 8** a<sub>1</sub>–a<sub>3</sub> 3D CLSM images and b<sub>1</sub>–b<sub>3</sub> particle spacing distribution of MWCNTs–FITC in EP after curing at 25, 40 and 80 °C.



unbalance derived from the temperature gradient gave the driving force for the intense thermal motion of MWCNTs–FITC during the curing process. Besides, the temperature gradient resulted in the local viscosity difference around MWCNTs–FITC in different areas of EP, which made the viscosity-induced motion of MWCNTs–FITC possible. The combinations of all these factors might accelerate the aggregation of MWCNTs–FITC through the Brown movement. Meanwhile, with the EP chemical microstructure changing from the linear pattern to the 3D crosslinked network, the uneven spatial distribution of MWCNTs–FITC was gradually fixed in EP matrix phase.

### Observation of MWCNTs–FITC@QFs/EP

The surface morphologies of desized QFs (d-QFs) and MWCNTs–FITC@QFs were examined by SEM and AFM. Here, MWCNTs–FITC@QFs containing 0.05 wt% MWCNTs–FITC in the EP sizing agent were used as the typical example. As shown in Fig. 9a<sub>1</sub>, the d-QFs represented a smooth surface with some superficial grooves, indicating that the commercial sizing agent has been removed from QFs. And it could be observed much clearer from 3D AFM topographical image that these grooves were parallelly distributed along the longitudinal direction of d-QFs (Fig. 9b<sub>1</sub>). For the SEM image of MWCNTs–FITC@QFs in Fig. 9a<sub>2</sub>, it was seen that these grooves

were filled and a layer of MWCNTs–FITC/EP was evenly coated on the surface of d-QFs, in which a large number of MWCNTs–FITC were scattered uniformly in different angles. In contrast, the surface roughness (Ra) was 72.3 nm for MWCNTs–FITC@QFs, which was increased by 58.2% compared with 45.7 nm for d-QFs. Normally, the enhancement in surface roughness could improve the interfacial adhesion through providing more contact points and increasing mechanical interlocking between QFs and polymer matrix in composites. Additionally, the TGA measurement in Fig. S4 manifested that the weight content of MWCNTs–FITC/EP sizing agent onto MWCNTs–FITC@QFs has been controlled to be ~ 1.9 wt%, which accorded with the value range of 1.0–2.0 wt% for the weight content of sizing agent on the commercial fibers [71, 72].

Moreover, the cross sections of MWCNTs–FITC@QFs/EP composites were observed by both SEM and TEM. As shown in Fig. 10a<sub>1</sub>, the region in circular shape represented QFs and the other section around it was the region of EP matrix. Nevertheless, the existence of MWCNTs–FITC onto QFs could not be clearly seen from SEM image. The signals for element C and Si were detected using EDS analysis along the yellow line on the cross section of MWCNTs–FITC@QFs/EP composites as shown in Fig. 10a<sub>1</sub>. The yellow line started from EP matrix and went through the interfacial phase of MWCNTs–FITC@QFs/EP to reach the bulk region of QFs. As

**Figure 9** SEM and AFM images of a<sub>1</sub>, b<sub>1</sub> d-QFs and a<sub>2</sub>, b<sub>2</sub> MWCNTs–FITC@QFs.

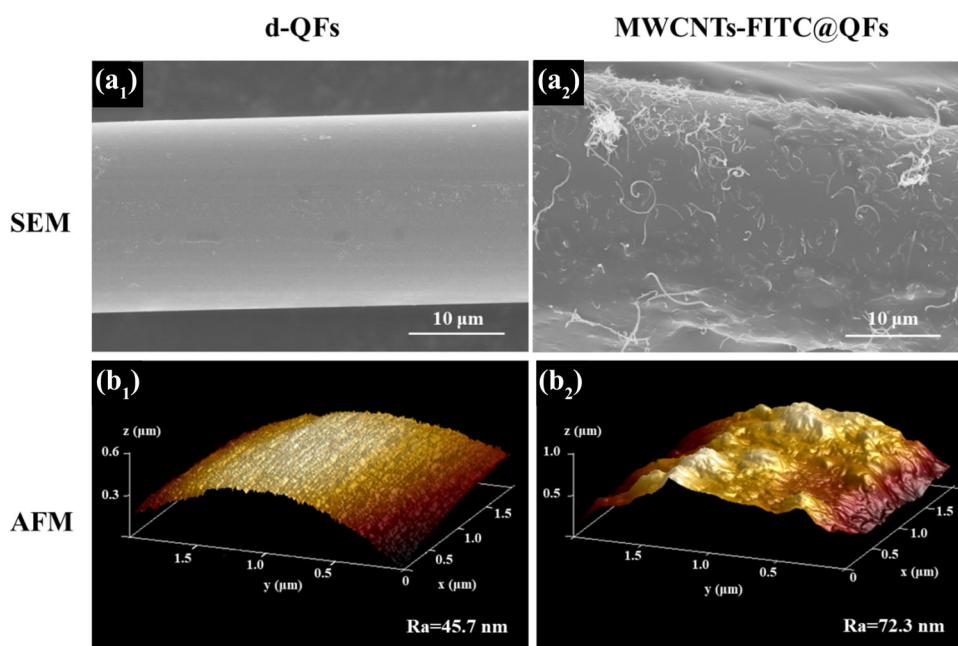
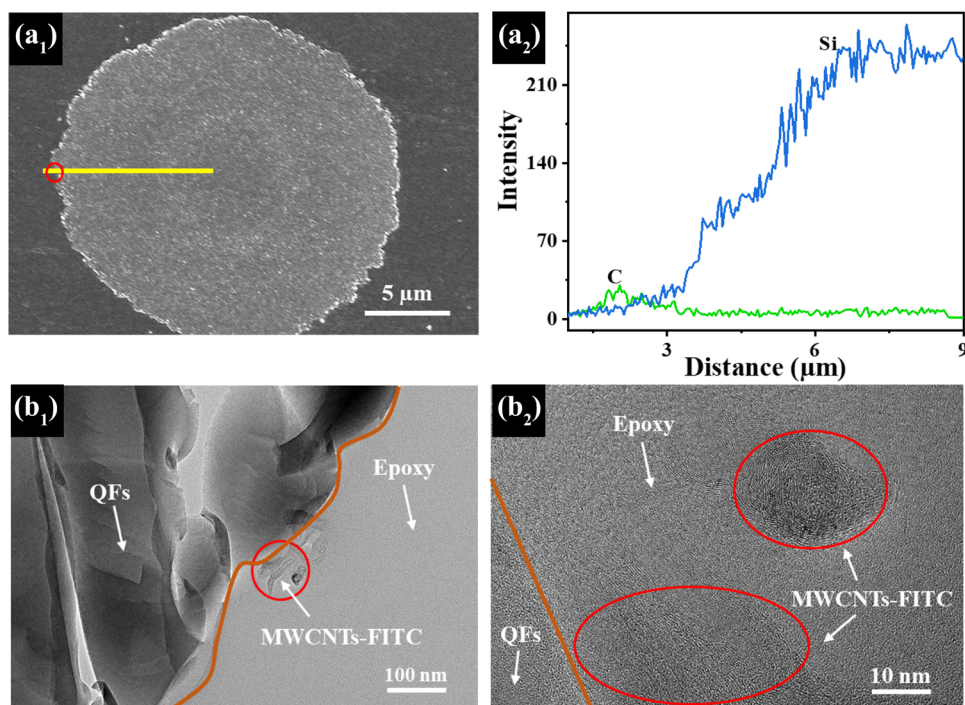


**Figure 10** **a**<sub>1</sub> SEM and **b**<sub>1</sub> TEM images of the cross sections of MWCNTs–FITC@QFs/EP composites, as well as **(a**<sub>2</sub>) EDS line profiles of element Si and C along the yellow line in panel **a**<sub>1</sub> and **b**<sub>2</sub> the corresponding high magnification of the local area in the red circle in panel **b**<sub>1</sub>.



shown in Fig. 10a<sub>2</sub>, the intensity of element Si significantly increased and kept at a high value level, confirming the main composition of QFs. Interestingly, the intensity of element C suddenly ascended in the interfacial phase of the composites and then descended in the bulk region of QFs to the level as in the EP region. This ascending in the intensity of element C proved the exact existence of MWCNTs–FITC in the interfacial phase of the composites. From TEM images of MWCNTs–FITC@QFs/EP composites in Fig. 10b<sub>1</sub>, QFs and EP matrix were observed as the dark and light sections, respectively. MWCNTs–FITC were obviously found in the interfacial phase as denoted in the red circle. MWCNTs–FITC were seen exiting in the form of aggregates from the magnified TEM image of local area in Fig. 10b<sub>2</sub>. However, the actual diffusion and macroscale spatial distribution of MWCNTs–FITC in the interfacial phase around QFs could not be in situ observed by TEM from the 3D view.

Based on the fluorescent feature of MWCNTs–FITC, it was assumed that MWCNTs–FITC could be directly observed in the interfacial phase of MWCNTs–FITC@QFs/EP composites by using CLSM. The 2D and 3D CLSM images of MWCNTs–FITC@QFs/EP composites are shown in Fig. 11. The contents of MWCNTs–FITC in the EP sizing agent were controlled to be 0.01, 0.05 and 0.10 wt,

respectively. As shown in Fig. 11a<sub>1</sub>, at the content of 0.01 wt%, MWCNTs–FITC were widely scattering on the surfaces of QFs. And some blank spots without MWCNTs–FITC were found, proving that the surfaces of QFs were not fully covered by MWCNTs–FITC at this low content. With MWCNTs–FITC content increasing to 0.05 wt%, the surfaces of QFs were fully covered by MWCNTs–FITC, emitting the green fluorescent light (Fig. 11a<sub>2</sub>). It seemed that MWCNTs–FITC gradually diffused into the EP matrix from the surfaces of QFs as indicated from the CLSM image inset in Fig. 11a<sub>2</sub>. When the MWCNTs–FITC content was as high as 0.10 wt%, both fluorescence-emitting MWCNTs–FITC and the blank spots were obviously detected on the surfaces of QFs as shown in Fig. 11a<sub>3</sub> and its inset. These blank spots should be derived from the aggregations of MWCNTs–FITC with high content value. Noticeably, the actual diffusion trend and spatial distribution of MWCNTs–FITC in the interfacial phase of MWCNTs–FITC@QFs/EP could be captured more clearly basing on the 3D CLSM images, which gave the direct information for the actual macro-dispersion state in a large-scale volume. As found from 3D CLSM images in Fig. 11b<sub>1</sub>–b<sub>3</sub>, MWCNTs–FITC diffused in form of aggregates instead of individual one, and such diffusion took place at the same time in a 3D space around QFs. And as found in Fig. 11b<sub>1</sub>–b<sub>3</sub>,



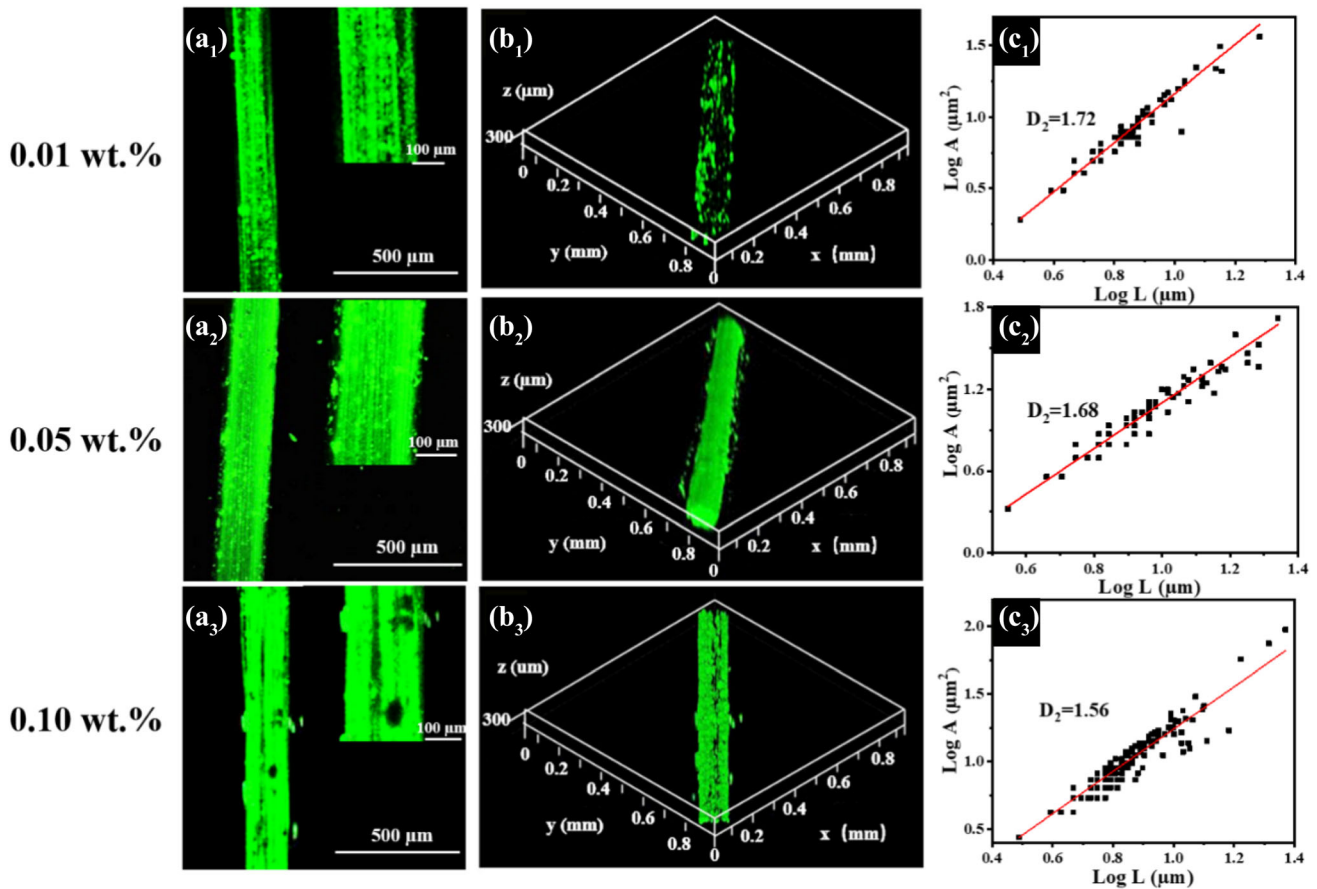


**Figure 11** a<sub>1</sub>–a<sub>3</sub> 2D and b<sub>1</sub>–b<sub>3</sub> 3D CLSM images of MWCNTs–FITC@QFs/EP composites along with c<sub>1</sub>–c<sub>3</sub> log A versus log L curve for MWCNTs–FITC. The contents of MWCNTs–FITC in

the sizing agent were controlled to be 0.01, 0.05 and 0.10 wt%, respectively. The insets in panel a<sub>1</sub>–a<sub>3</sub> are the corresponding high-magnification CSLM images.

the size of MWCNTs–FITC aggregates apparently increased with their content, thereby leading to the formation of aggregate block with much bigger size at 0.10 wt% content. The aggregated state of MWCNTs–FITC could be also characterized with 2D fractal dimension  $D_2$ . As shown in Fig. 11c<sub>1</sub>–c<sub>3</sub>, the  $D_2$  values of MWCNTs–FITC were calculated to be 1.72, 1.68 and 1.56 for the cases with contents of 0.01, 0.05 and 0.10 wt% in the sizing agent, respectively. The lower  $D_2$  value meant that the aggregated structure of MWCNTs–FITC was not much dense, which would generate adverse effect on the diffusion of MWCNTs–FITC in the interfacial phase between QFs and EP. It was found in Fig. 11 that such diffusion in a 3D large-scale space was more obvious for the case with 0.05 wt% MWCNTs–FITC in the sizing agent. Thus, MWCNTs–FITC@QFs containing 0.05 wt% MWCNTs–FITC in the EP sizing agent were selected in the following study.

The effect of the curing temperature on the diffusion state of MWCNTs–FITC in the interfacial phase between MWCNTs–FITC@QFs and EP was also evaluated here. As shown in Fig. 12, with the curing temperature increasing, more and more MWCNTs–FITC diffused into EP matrix through a longer distance from QFs. The actual macro-dispersion and diffusion state in a large-scale volume around QFs were seen more clearly from 3D CLSM images (Fig. 12b<sub>1</sub>–b<sub>3</sub>). The ascending in the curing temperature provided more driving force for MWCNTs–FITC to move from their high content region in the interfacial phase of MWCNTs–FITC@QFs/EP to the blank region in EP matrix. Besides, the size and microstructure of MWCNTs–FITC aggregates also evolved with the curing temperature. The  $D_2$  values of MWCNTs–FITC were calculated to be 1.70, 1.68 and 1.63, respectively, at the curing temperatures of 25, 40 and 80 °C. The lower  $D_2$  value meant that the aggregated structure of MWCNTs–FITC was not

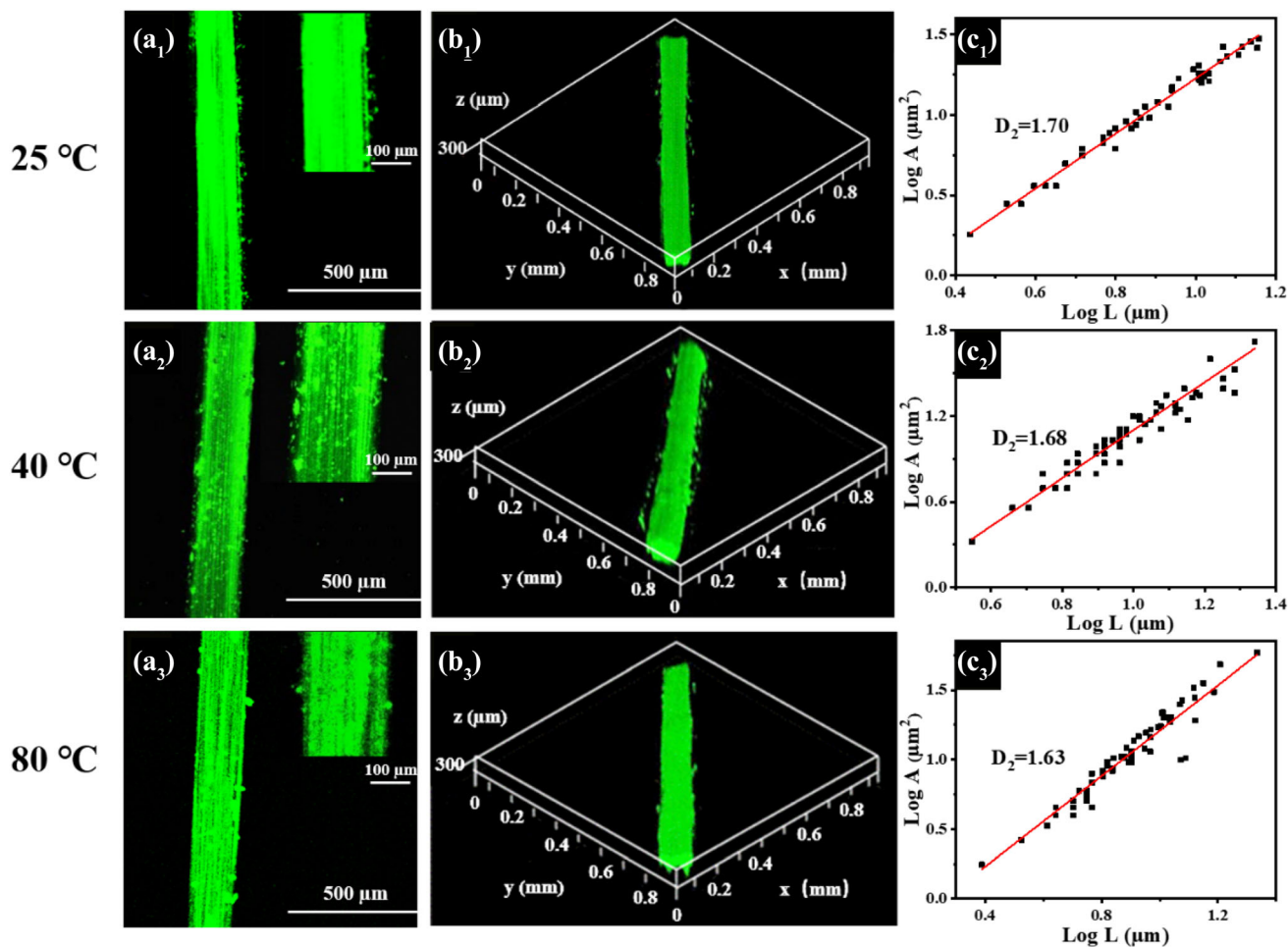


**Figure 12**  $a_1$ – $a_3$  2D and  $b_1$ – $b_3$  3D CLSM images of MWCNTs–FITC@QFs along with  $c_1$ – $c_3$  log  $A$  versus log  $L$  curve for MWCNTs–FITC. The curing temperatures of MWCNTs–

FITC@QFs/EP were controlled to be 25, 40 and 80 °C, respectively. The insets in panel  $a_1$ – $a_3$  are the corresponding high-magnification CSLM images.

dense, which would limit the diffusion of MWCNTs–FITC into EP matrix. It was obvious that the high curing temperature would promote the self-assembly and aggregation of MWCNTs–FITC. According to Eqs. (4) and (5), the theoretical diffusion coefficient  $D_{NP}$  of MWCNTs–FITC and mean square displacement among MWCNTs–FITC in the interfacial phase of MWCNTs–FITC@QFs/EP composites at different curing temperatures were calculated by measuring the viscosity and gel time (Labeled as  $\Delta t$ ) of EP matrix and hydrodynamic size (labeled as  $\phi$ ) of MWCNTs–FITC aggregates. Here, the hydrodynamic size of MWCNTs–FITC was measured by DLS. As listed in Table 3, the value of theoretical average diffusion distance  $\bar{l}_t$  was highest at 40 °C. And the value range of theoretical average diffusion distance was basically consistent with that of the actual

average diffusion distance measured from CLSM images. This proved that the diffusion coefficient  $D_{NP}$  and diffusion distance of MWCNTs–FITC from the interfacial phase into EP matrix at different curing temperatures could be well described by SPT and Einstein’s Stokes theories on basis of fluorescence imaging characterization.

The aforementioned results revealed that the macroscale 3D diffusion and spatial distribution of MWCNTs–FITC in the interfacial phase of MWCNTs–FITC@QFs/EP composites could be directly observed by CLSM due to the fluorescent feature of MWCNTs–FITC. After concluding these visual results, the morphological diffusion mechanism of MWCNTs–FITC in the interfacial phase of MWCNTs–FITC@QFs/EP composites is illustrated in Fig. 13. Under the thermal condition, the heat was

**Table 3** The diffusion coefficient  $D_{NP}$ , theoretical average diffusion distance  $\bar{l}_t$  and measured average diffusion distance  $\bar{l}_m$  of MWCNTs–FITC away from QFs at curing temperatures of 25, 40 and 80 °C

$T$ (°C)	$\phi$ (μm)	$\eta$ (Pa s)	$\Delta t$ (min)	$D_{NP}$ (m <sup>2</sup> /s)	$\bar{l}_t$ (μm)	$\bar{l}_m$ (μm)
25	1.2	0.35	180	$1.04 \times 10^{-15}$	4.7	4.2
40	1.5	0.20	145	$1.53 \times 10^{-15}$	5.2	6.3
80	2.3	0.12	40	$1.87 \times 10^{-15}$	3.0	3.5

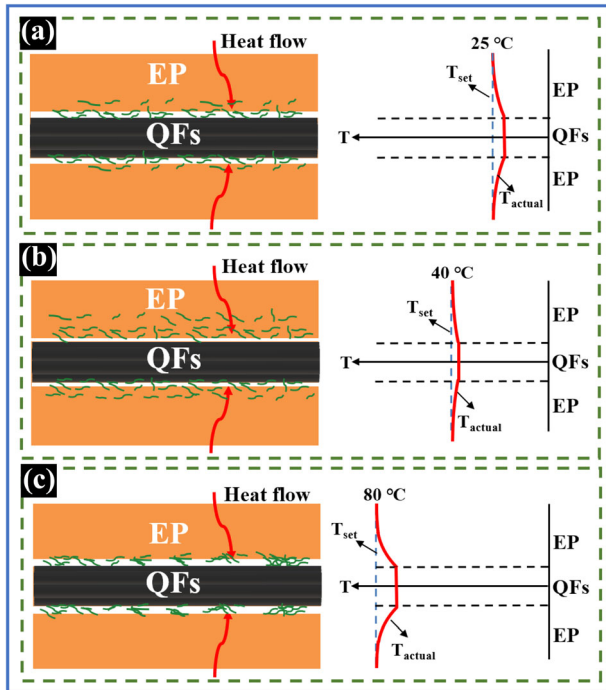


**Figure 13** Mechanism for the diffusion and distribution of MWCNTs–FITC in the interfacial phase of MWCNTs–FITC@QFs/EP composites at curing temperatures of 25, 40 and 80 °C.

gradually conducted from the outside to the inside of MWCNTs–FITC@QFs/EP composites. The temperature gradient would definitely exist in the composites, which could be mainly divided into three regions including EP matrix phase with high temperature, MWCNTs–FITC@QFs/EP interfacial phase with moderate temperature and QFs bulk phase with relatively lower temperature as indicated in Fig. 13. Noticeably, since MWCNTs were a kind of excellent conductor in transferring heat, it could be predicted that the distribution state of MWCNTs–FITC in the interfacial phase would affect the temperature gradient at this local area. In detail, at the low curing temperature of 25 °C, the size of MWCNTs–FITC aggregates was small and the gel time of EP matrix

was long due to its low reactivity, which provided long enough time window for MWCNTs–FITC to diffuse from the QFs surface into the interfacial phase as driven by their content gradient. Reasonably, limited by the high viscosity of EP matrix and low thermally driven Brown motion, it was difficult for MWCNTs–FITC to diffuse into EP matrix. In this case, the temperature gradient difference between EP matrix and QFs bulk was relatively small (Fig. 13a), as a result of the relatively uniform distributed MWCNTs–FITC in the interfacial phase as observed in Fig. 12a<sub>1</sub>. As the curing temperature increasing to 40 °C along with the EP viscosity decreasing, MWCNTs–FITC could diffuse from their high content region on QFs surfaces into the interfacial phase and then into the blank region in EP matrix phase, upon the combining functions of nanoparticle interactions, thermally driven microscale Brown motion and thermodynamic environment changing. A better thermally conducting network of MWCNTs–FITC was formed in the interfacial phase, which much contributed to the further reduction in the temperature gradient difference between EP matrix and QFs bulk (Fig. 13b). Simultaneously, this temperature gradient difference would promote the continuous diffusion and uniform distribution of MWCNTs–FITC in the interfacial phase and in EP matrix phase. However, when the curing temperature was elevated to as high as 80 °C, the size and number of MWCNTs–FITC aggregates increased sharply as seen in Fig. 12a<sub>3</sub>–b<sub>3</sub>, due to the thermally induced self-assembly and the intensified interactions among MWCNTs–FITC. The big-sized MWCNTs–FITC aggregates gathered in the interfacial phase and formed large blocks against their diffusion into EP matrix phase. Even though the viscosity of EP matrix was reduced a lot, the uneven spatial distribution of MWCNTs–FITC was quickly fixed in the interfacial phase along with 3D crosslinked microstructure formation of cured EP, due to the high reactivity and

short gel time of EP resin at the high temperature. Therefore, the temperature gradient difference from EP matrix phase to QFs bulk phase was obvious as presented in Fig. 13c, which was attributed to the nonuniform thermally conducting network of MWCNTs–FITC aggregates in the interfacial phase.

## Conclusions

In this study, fluorescein isothiocyanate covalently labeled MWCNTs (MWCNTs–FITC) were successfully synthesized through sequent reactions of the intermediate product MWCNTs–PGMA with ethylenediamine and then with FITC. Through in-depth research on the dispersion mechanism of MWCNTs–FITC in the EP matrix and QFs/EP interfacial phases, the following conclusions were obtained: First of all, the PGMA component in the grafting layer played a decisive role in endowing the green fluorescent feature to MWCNTs by protecting FITC from the direct contact with highly electrically conductive carbon nano tubes. Based on this, the macroscale 3D spatial dispersion of MWCNTs–FITC in the EP matrix and in the interfacial phases of QFs/EP composites was in situ observed via fluorescent imaging in a noninvasive way. Secondly, in considering the affecting factors of MWCNTs–FITC content and curing temperature, the dispersion state of MWCNTs–FITC in the EP matrix phase was quantitatively evaluated using Morisita's index ( $I$ ) and particle spacing probability density theory, while the diffusion behavior of MWCNTs–FITC in the interfacial phase was examined using 2D fractal dimension and Einstein's Stokes theory. Due to the interactions of inter-particle van der Waals forces and physical entanglement, the content of 0.05 wt% was the threshold for uniform dispersion of MWCNTs–FITC. The particle spacing coefficient of MWCNTs–FITC as high as 1.69 was achieved curing at 25 °C, corresponding to the well dispersion of MWCNTs–FITC in the matrix, while for the dispersion at QFs/EP interface, the optimal curing temperature was 40 °C where the actual average diffusion distance ( $\bar{l}_m$ ) was as high as 6.3  $\mu\text{m}$ . Finally, the generality of the established quantification method in the present study provided potential realistic feasibility to in situ characterize macroscale 3D spatial dispersion of inorganic nanofillers in polymer-based composites via fluorescence imaging.

## Acknowledgements

The authors are very pleased to acknowledge financial support from Beijing Natural Science Foundation (Grant No. 2192044), National Key R&D Program of China (No. 2019YFB1504800), Fundamental Research Funds for the Central Universities (Grant No. XK1802-2), BUCT Youth Talent Plan, 2020 Open Project of State Key Laboratory of Organic-Inorganic Composites (Grant No. Oic-202001008), Consulting Research Project of Chinese Academy of Engineering (No. 2020-XY-81), National Natural Science Foundation of China (Grant No. U1362205, 5157031049, 51373016) and Natural Science Foundation of Jiangsu Province (Grant No. SBK2014040489).

## Declarations

**Conflict of interest** We declare that we have no financial and personal relationships with other people or organizations that can inappropriately influence our work; there is no professional or other personal interest of any nature or kind in any product, service and/or company that could be construed as influencing the position presented in, or the review of, the manuscript entitled.

**Supplementary Information:** The online version contains supplementary material available at <http://doi.org/10.1007/s10853-021-06350-x>.

## References

- [1] Vryonis O, Andritsch T, Vaughan AS, Lewin PL (2019) An alternative synthesis route to graphene oxide: influence of surface chemistry on charge transport in epoxy-based composites. *J Mater Sci* 54:8302–8318. <https://doi.org/10.1007/s10853-019-03477-w>
- [2] Nie H-J, Xu Z, Tang B-L, Dang C-Y, Yang Y-R, Zeng X-L (2021) The effect of graphene oxide modified short carbon fiber on the interlaminar shear strength of carbon fiber fabric/epoxy composites. *J Mater Sci* 56:488–496. <https://doi.org/10.1007/s10853-020-05286-y>
- [3] Gao Y, Jing H, Zhou Z, Chen W, Li L, Shi X (2020) Graphene oxide-assisted multi-walled carbon nanotube reinforcement of the transport properties in cementitious composites. *J Mater Sci* 55:603–618. <https://doi.org/10.1007/s10853-019-04040-3>
- [4] Kumar A, Sharma K, Dixit AR (2020) Carbon nanotube- and graphene-reinforced multiphase polymeric composites:

- review on their properties and applications. *J Mater Sci* 55:2682–2724. <https://doi.org/10.1007/s10853-019-04196-y>
- [5] Aslan A, Salur E, Düzcükoğlu H, Şahin ÖS, Ekrem M (2021) The effects of harsh aging environments on the properties of neat and MWCNT reinforced epoxy resins. *Construct Build Mater* 272:121929. <https://doi.org/10.1016/j.conbuildmat.2020.121929>
- [6] Gu H, Zhang H, Ma C, Xu X, Wang Y, Wang Z (2019) Trace electrosprayed nanopolystyrene facilitated dispersion of multiwalled carbon nanotubes: simultaneously strengthening and toughening epoxy. *Carbon* 142:131–140
- [7] Pantano A, Montinaro N, Cerniglia D, Micciulla F, Bistarelli S, Cataldo A (2019) Novel non-destructive evaluation technique for the detection of poor dispersion of carbon nanotubes in nanocomposites. *Compos B Eng* 163:52–58
- [8] Wang M, Ma L, Shi L, Feng P, Wang X, Zhu Y (2019) Chemical grafting of nano-SiO<sub>2</sub> onto graphene oxide via thiol-ene click chemistry and its effect on the interfacial and mechanical properties of GO/epoxy composites. *Compos Sci Technol* 182:107751. <https://doi.org/10.1016/j.compscitech.2019.107751>
- [9] Scaffaro R, Maio A (2019) Integrated ternary bionanocomposites with superior mechanical performance via the synergistic role of graphene and plasma treated carbon nanotubes. *Compos B Eng* 168:550–559
- [10] Zhang C, Tang Z, Guo B, Zhang L (2019) Concurrently improved dispersion and interfacial interaction in rubber/nanosilica composites via efficient hydrosilane functionalization. *Compos Sci Technol* 169:217–223
- [11] Montinaro N, Fustaino M, Pantano A (2020) Carbon nanotubes dispersion assessment in nanocomposites by means of a pulsed thermographic approach. *Materials* 13:5649. <https://doi.org/10.3390/ma13245649>
- [12] Raimondo M, Naddeo C, Vertuccio L, Lafdi K, Sorrentino A, Guadagno L (2019) Carbon-based aeronautical epoxy nanocomposites: effectiveness of atomic force microscopy (AFM) in investigating the dispersion of different carbonaceous nanoparticles. *Polymers* 11:832. <https://doi.org/10.3390/polym11050832>
- [13] Xia T, Guo X, Lin Y, Xin B, Li S, Yan N (2019) Aggregation of oxidized multi-walled carbon nanotubes: interplay of nanomaterial surface O-functional groups and solution chemistry factors. *Environ Pollut* 251:921–929
- [14] Li F, Li L, Zhong G, Zhai Y, Li Z (2019) Effects of ultrasonic time, size of aggregates and temperature on the stability and viscosity of Cu-ethylene glycol (EG) nanofluids. *Int J Heat Mass Transfer* 129:278–286
- [15] Rodríguez HA, Kriven WM, Casanova H (2019) Development of mechanical properties in dental resin composite: effect of filler size and filler aggregation state. *Mater Sci Eng C* 101:274–282
- [16] Kobashi K, Sekiguchi A, Yamada T, Muroga S, Okazaki T (2020) Dispersions of high-quality carbon nanotubes with narrow aggregate size distributions by viscous liquid for conducting polymer composites. *ACS Appl Nano Mater* 3:1391–1399
- [17] Ghoderao P, Sahare S, Alegaonkar P, Kulkarni AA, Bhavne T (2018) Multiwalled carbon nanotubes decorated with Fe<sub>3</sub>O<sub>4</sub> nanoparticles for efficacious doxycycline delivery. *ACS Appl Nano Mater* 2:607–616
- [18] Zhao Z, Katai H, Higashi K, Ueda K, Kawakami K, Moribe K (2019) Cryo-TEM and AFM observation of the time-dependent evolution of amorphous probucol nanoparticles formed by the aqueous dispersion of ternary solid dispersions. *Mol Pharm* 16:2184–2198
- [19] Schneider S, Lefebvre J, Diercks NJ, Berger FJ, Fo Lapointe, Schleicher J (2020) Phenanthroline additives for enhanced semiconducting carbon nanotube dispersion stability and transistor performance. *ACS Appl Nano Mater*. <https://doi.org/10.1021/acsanm.0c02813>
- [20] Sun L, Zhang D, Sun Y, Wang S, Cai J (2018) Facile fabrication of highly dispersed Pd@ Ag core-shell nanoparticles embedded in spirulina platensis by electroless deposition and their catalytic properties. *Adv Funct Mater* 28:1707231. <https://doi.org/10.1002/adfm.201707231>
- [21] Hanifah MFR, Jaafar J, Othman M, Ismail A, Rahman M, Yusof N (2019) One-pot synthesis of efficient reduced graphene oxide supported binary Pt-Pd alloy nanoparticles as superior electro-catalyst and its electro-catalytic performance toward methanol electro-oxidation reaction in direct methanol fuel cell. *J Alloys Compd* 793:232–246
- [22] Liu X, Bu Y, Cheng T, Gao W, Jiang Q (2019) Flower-like carbon supported Pd–Ni bimetal nanoparticles catalyst for formic acid electrooxidation. *Electrochim Acta* 324:134816. <https://doi.org/10.1016/j.electacta.2019.134816>
- [23] Zhao F, Ling L, Liu L, Zafar A, Ni Z (2017) The dispersion of graphene in conductive epoxy composites investigated by Raman spectroscopy. *J Raman Spectrosc* 48:432–436
- [24] Chen M, Fan G, Tan Z, Yuan C, Xiong D, Guo Q (2019) Tailoring and characterization of carbon nanotube dispersity in CNT/6061Al composites. *Mater Sci Eng A* 757:172–181
- [25] Rishi K, Narayanan V, Beaucage G, McGlasson A, Kuppa V, Ilavsky J (2019) A thermal model to describe kinetic dispersion in rubber nanocomposites: the effect of mixing time on dispersion. *Polymer* 175:272–282
- [26] Löf D, Hamieau G, Zalich M, Ducher P, Kynde S, Midtgaard SR (2020) Dispersion state of TiO<sub>2</sub> pigment particles studied by ultra-small-angle X-ray scattering revealing dependence on dispersant but limited change during drying of paint

- coating. *Prog Org Coat* 142:105590. <https://doi.org/10.1016/j.porgcoat.2020.105590>
- [27] Chen K, Kang M, Lu A, Chen L, Song L, Sun R (2019) Visualization of silica dispersion states in silicone rubber by fluorescent labeling. *J Mater Sci* 54:5149–5159. <https://doi.org/10.1007/s10853-018-03191-z>
- [28] Lv X, Kang M, Chen K, Yuan L, Shen S, Sun R (2020) Preparation of fluorescent calcium carbonate and visualization of its dispersion states in polypropylene. *J Compos Mater* 54:913–921
- [29] Guan W, Wang S, Lu C, Tang BZ (2016) Fluorescence microscopy as an alternative to electron microscopy for microscale dispersion evaluation of organic–inorganic composites. *Nat Commun* 7:11811. <https://doi.org/10.1038/ncomms11811>
- [30] Hackley PC, Jubb AM, Burruss RC, Beaven AE (2020) Fluorescence spectroscopy of ancient sedimentary organic matter via confocal laser scanning microscopy (CLSM). *Int J Coal Geol* 223:103445. <https://doi.org/10.1016/j.coal.2020.103445>
- [31] Teng X, Li F, Lu C (2020) Visualization of materials using the confocal laser scanning microscopy technique. *Chem Soc Rev* 49:2408–2425
- [32] Wang C, Hao Y, Wang Y, Song H, Hussain S, Gao R (2021) Multiwall carbon nanotubes non-covalently functionalized by porphyrin–sn networks for protein adsorption. *ACS Appl Nano Mater*. <https://doi.org/10.1021/acsnm.0c03215>
- [33] Ballesteros B, de la Torre G, Ehli C, Aminur Rahman G, Agulló-Rueda F, Guldi DM (2007) Single-wall carbon nanotubes bearing covalently linked phthalocyanines photoinduced electron transfer. *J Am Chem Soc* 129:5061–5068
- [34] Siddiqui AS, Hayat A, Nawaz MH, Ahmad MA, Nasir M (2020) Effect of sulfur doping on graphene oxide towards amplified fluorescence quenching based ultrasensitive detection of hydrogen peroxide. *Appl Surf Sci* 509:144695. <https://doi.org/10.1016/j.apsusc.2019.144695>
- [35] Zhang M, Wang W, Wu F, Yuan P, Chi C, Zhou N (2017) Magnetic and fluorescent carbon nanotubes for dual modal imaging and photothermal and chemo-therapy of cancer cells in living mice. *Carbon* 123:70–83
- [36] Lorne T, Jiménez-Ruiz M, Rols S, Escudier J-M, Rubio-Zuazo J, Zbiri M (2017) Competition between covalent and non-covalent grafting of fluorescein isothiocyanate on double-walled carbon nanotubes: a quantitative approach. *Carbon* 123:735–743
- [37] Kumawat MK, Thakur M, Bahadur R, Kaku T, Prabhuraj R, Ninawe A (2019) Preparation of graphene oxide-graphene quantum dots hybrid and its application in cancer theranostics. *Mater Sci Eng C* 103:109774. <https://doi.org/10.1016/j.msec.2019.109774>
- [38] Ilčíková M, Danko M, Doroshenko M, Best A, Mrlik M, Csomorová K (2016) Visualization of carbon nanotubes dispersion in composite by using confocal laser scanning microscopy. *Eur Polym J* 79:187–197
- [39] Zhang R, Shang T, Yang G, Jia X, Cai Q, Yang X (2016) Direct fabrication of hybrid nanofibres composed of SiO<sub>2</sub>-PMMA nanospheres via electrospinning. *Colloids Surf B* 144:238–249
- [40] Jia X, Li W, Xu X, Li W, Cai Q, Yang X (2015) Numerical characterization of magnetically aligned multiwalled carbon nanotube–Fe<sub>3</sub>O<sub>4</sub> nanoparticle complex. *ACS Appl Mater Interfaces* 7:3170–3179
- [41] Adnan MM, Tveten EG, Glaum J, Ese MHG, Hvidsten S, Glomm W (2019) Epoxy-based nanocomposites for high-voltage insulation: a review. *Adv Electron Mater* 5:1800505. <https://doi.org/10.1002/aelm.201800505>
- [42] Zhang L, Chen Z, Mao J, Wang S, Zheng Y (2020) Quantitative evaluation of inclusion homogeneity in composites and the applications. *J Mater Res Technol* 9:6790–6807
- [43] Luo Z, Koo JH (2007) Quantifying the dispersion of mixture microstructures. *J Microsc* 225:118–125
- [44] Shin JI, Cho SJ, Jeon J, Lee KH, Wie JJ (2019) Three-dimensional micropatterning of semiconducting polymers via capillary force-assisted evaporative self-assembly. *Soft Matter* 15:3854–3863
- [45] Jiang S, Zhao J, Förster R, Weidlich S, Plidschun M, Kobelke J (2020) Three dimensional spatiotemporal nanoscale position retrieval of the confined diffusion of nano-objects inside optofluidic microstructured fibers. *Nanoscale* 12:3146–3156
- [46] Sutter E, Zhang B, Sutter S, Sutter P (2019) In situ electron microscopy of the self-assembly of single-stranded DNA-functionalized Au nanoparticles in aqueous solution. *Nanoscale* 11:34–44
- [47] Karatrantos A, Composto RJ, Winey KI, Clarke N (2019) Nanorod diffusion in polymer nanocomposites by molecular dynamics simulations. *Macromolecules* 52:2513–2520
- [48] Barcia FL, Amaral TP, Soares BG (2003) Synthesis and properties of epoxy resin modified with epoxy-terminated liquid polybutadiene. *Polymer* 44:5811–5819
- [49] Huang Z, Ma Y, Jing W, Zhang Y, Jia X, Cai Q (2020) Tracing carbon nanotubes (CNTs) in rat peripheral nerve regenerated with conductive conduits composed of poly (lactide-co-glycolide) and fluorescent CNTs. *ACS Biomater Sci Eng* 6:6344–6355
- [50] Niu Y, Wang H (2019) Dielectric nanomaterials for power energy storage: surface modification and characterization. *ACS Appl Nano Mater* 2:627–642
- [51] Wang X, Chen D, Zhong W, Zhang L, Fan X, Cai Z (2020) Experimental and theoretical evaluations of the interfacial

- interaction between carbon nanotubes and carboxylated butadiene nitrile rubber: mechanical and damping properties. *Mater Des* 186:108318. <https://doi.org/10.1016/j.matdes.2019.108318>
- [52] Vryonis O, Andritsch T, Vaughan AS, Lewin PL (2020) Effect of surfactant molecular structure on the electrical and thermal performance of epoxy/functionalized-graphene nanocomposites. *Polym Compos* 41:2753–2767
- [53] Ren J, Yu D, Feng L, Wang G, Lv G (2017) Nanocable-structured polymer/carbon nanotube composite with low dielectric loss and high impedance. *Compos Part A Appl Sci Manuf* 98:66–75
- [54] Kaewsaneha C, Opaprakasit P, Polpanich D, Smanmoo S, Tangboriboonrat P (2012) Immobilization of fluorescein isothiocyanate on magnetic polymeric nanoparticle using chitosan as spacer. *J Colloid Interface Sci* 377:145–152
- [55] Kundele EV, Tepliakov NV, Leonov MY, Maslov VG, Baranov AV, Fedorov AV (2019) Amino functionalization of carbon dots leads to red emission enhancement. *J Phys Chem Lett* 10:5111–5116
- [56] Hirata E, Yudasaka M, Ushijima N, Sakaguchi N, Maeda Y, Tanaka T (2019) Fate of Carbon Nanotubes Locally Implanted in Mice Evaluated by Near-Infrared Fluorescence Imaging: Implications for Tissue Regeneration. *ACS Appl Nano Mater* 2:1382–1390
- [57] Chiu CF, Dementev N, Borguet E (2011) Fluorescence quenching of dyes covalently attached to single-walled carbon nanotubes. *J Phys Chem A* 115:9579–9584
- [58] Yang H, Pan S, Ma D, He D, Wang Y, Xie S (2016) Light-harvesting dendrimer zinc-phthalocyanines chromophores labeled single-wall carbon nanotube nanoensembles: Synthesis and photoinduced electron transfer. *J Lumin* 179:588–594
- [59] Subramanian N, Rai A, Chattopadhyay A (2017) Atomistically derived cohesive behavior of interphases in carbon fiber reinforced CNT nanocomposites. *Carbon* 117:55–64
- [60] Cui S, Li L, Wang Q (2020) Improved molecular chain constraint of poly (propylene carbonate) composites by the synergistic effect of poly (vinyl alcohol) and carbon nanotubes. *Compos B Eng* 194:108074. <https://doi.org/10.1016/j.compositesb.2020.108074>
- [61] Imre AR (2006) Artificial fractal dimension obtained by using perimeter–area relationship on digitalized images. *Appl Math Comput* 173:443–449
- [62] Florio BJ, Fawell PD, Small M (2019) The use of the perimeter-area method to calculate the fractal dimension of aggregates. *Powder Technol* 343:551–559
- [63] Zhang J, Yang M, Mazi W, Adhikari K, Fang M, Xie F (2016) Unusual fluorescent responses of morpholine-functionalized fluorescent probes to pH via manipulation of BODIPY's HOMO and LUMO energy orbitals for intracellular pH detection. *ACS Sens* 1:158–165
- [64] Wang J, Liao K-S, Früchtl D, Tian Y, Gilchrist A, Alley NJ (2012) Nonlinear optical properties of carbon nanotube hybrids in polymer dispersions. *Mater Chem Phys* 133:992–997
- [65] Basiuk EV, Huerta L, Basiuk VA (2019) Noncovalent bonding of 3d metal (II) phthalocyanines with single-walled carbon nanotubes: a combined DFT and XPS study. *Appl Surf Sci* 470:622–630
- [66] Campidelli S, Sooambar C, Lozano Diz E, Ehli C, Guldi DM, Prato M (2006) Dendrimer-functionalized single-wall carbon nanotubes: synthesis, characterization, and photoinduced electron transfer. *J Am Chem Soc* 128:12544–12552
- [67] Zhang W, Li H, Gao L, Zhang Q, Zhong W, Sui G (2018) Molecular simulation and experimental analysis on thermal and mechanical properties of carbon nanotube/epoxy resin composites with different curing agents at high-low temperature. *Polym Compos* 39:E945–E954
- [68] Pimenta Teixeira K, Perdigão Rocha I, De Sá CL, Flores J, Dauer EA, Ghahremaninezhad A (2016) The effect of curing temperature on the properties of cement pastes modified with TiO<sub>2</sub> nanoparticles. *Materials* 9:952. <https://doi.org/10.3390/ma9110952>
- [69] Charlot B, Desgarceaux R, Giani A, Bardin F (2017) PLL-FITC fluorescence thermography on dry surfaces. In: 2017 Symposium on design, test, integration and packaging of MEMS/MOEMS (DTIP)IEEE, pp 1–5
- [70] Imhof A, Megens M, Engelberts J, De Lang D, Sprik R, Vos W (1999) Spectroscopy of fluorescein (FITC) dyed colloidal silica spheres. *J Phys Chem B* 103:1408–1415
- [71] Ma L, Zhu Y, Feng P, Song G, Huang Y, Liu H (2019) Reinforcing carbon fiber epoxy composites with triazine derivatives functionalized graphene oxide modified sizing agent. *Compos B Eng* 176:107078. <https://doi.org/10.1016/j.compositesb.2019.107078>
- [72] Li L, Yan C, Xu H, Liu D, Shi P, Zhu Y (2019) Improving the interfacial properties of carbon fiber–epoxy resin composites with a graphene-modified sizing agent. *J Appl Polym Sci* 136:47122

**Publisher's Note** Springer Nature remains neutral with regard to jurisdictional claims in published maps and institutional affiliations.